ACS OMEGA

http://pubs.acs.org/journal/acsodf

Article

From Low to High Saturation Magnetization in Magnetite Nanoparticles: The Crucial Role of the Molar Ratios Between the Chemicals

Yaser Hadadian, Hajar Masoomi, Ali Dinari, Chiseon Ryu, Seong Hwang, Seokjae Kim, Beong ki Cho, Jae Young Lee,* and Jungwon Yoon*

Cite This: *ACS Omega* 2022, 7, 15996−16012

Read Online

ACCESS | Metrics & More | Article Recommendations | Supporting Information

ABSTRACT: In this study, a comprehensive characterization of iron oxide nanoparticles synthesized by using a simple one-pot thermal decomposition route is presented. In order to obtain monodisperse magnetite nanoparticles with high saturation magnetization, close to the bulk material, the molar ratios between the starting materials (solvents, reducing agents, and surfactants) were varied. Two out of nine conditions investigated in this study resulted in monodisperse iron oxide nanoparticles with high saturation magnetization (90 and 93% of bulk magnetite). The X-ray diffraction analyses along with the inspection of the lattice structure through transmission electron micrographs revealed that the main cause of the reduced magnetization in the other seven samples is likely due to the presence of distortion and microstrain in the particles. Although the thermogravimetric analysis, Raman and Fourier transform infrared spectroscopies confirmed the presence of covalently bonded oleic acid on the surface of all the samples, the particles with higher polydispersity and the lowest surface coating molecules showed the lowest saturation magnetization. Based on the observed results, it could be speculated that the changes in the kinetics of the reactions, induced by varying the molar ratio of the starting chemicals, can lead to the production of the particles with higher polydispersity and/or lattice deformation in their crystal structures. Finally, it was concluded that the experimental conditions for obtaining high-quality iron oxide nanoparticles, particularly the molar ratios and the heating profile, should not be chosen independently; for any specific molar ratio, there may exist a specific heating profile or vice versa. Because this synthetic consideration has rarely been reported in the literature, our results can give insights into the design of iron oxide nanoparticles with high saturation magnetization for different applications.

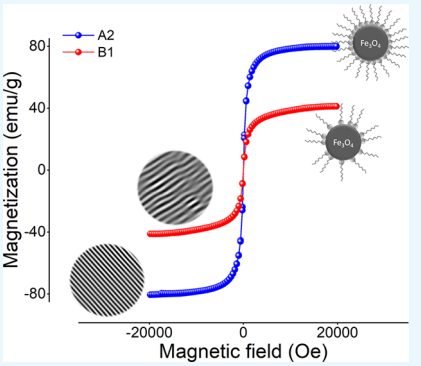

1. INTRODUCTION

Among 16 types of iron oxides, magnetite and maghemite, due to their unique magnetic properties, have always received substantial attention. Particularly, with the emergence of nanoscience and nanotechnology, they have gained fundamental interest and been used widely for technological applications in several areas including data storage, spintronics, biology, and medicine. Consequently, research on the synthesis of these two types of iron oxides has also been intensively developed in the past 2 decades. However, because of their peculiar size/shape-dependent magnetic properties, reaching the bulk saturation magnetization values in nanoscale particles remains challenging.

Magnetite ($Fe^{2+}Fe_2^{3+}O_4$), in its bulk state, has a cubic inverse spinel structure with a lattice parameter of 8.39 Å, wherein all the divalent cations occupy octahedral sites and trivalent irons are equally distributed into octahedral and tetrahedral sites.[1] On the other hand, in maghemite ($\gamma-Fe_2O_3$), with a lattice parameter of 8.34 Å, all the cations are trivalent irons, and the compensation of Fe^{2+} oxidation happens through the occurrence of the vacancies in its structure.[2,3] In both structures, the antiferromagnetic (superexchange interaction) coupling between the cations in octahedral and tetrahedral sites occurs through oxygen anions, and the net magnetic moment originates from the difference between the number of spins in these two sublattices. However, because of the vacancies in maghemite and the difference between the arrangement of cations in octahedral and tetrahedral sites, theoretical calculations for stoichiometric bulk samples indicate that the magnetic moment per unit formula of magnetite (4 Bohr magnetons, μ_B) is larger than that of maghemite (2.5 μ_B).[1] Considering this and its higher susceptibility, magnetite is preferred in many applications

Received: February 25, 2022
Accepted: April 12, 2022
Published: April 28, 2022

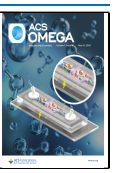

https://doi.org/10.1021/acsomega.2c01136
ACS Omega 2022, 7, 15996−16012

including biomedical uses. However, synthesizing highly stable and monodisperse magnetite nanoparticles displaying bulk-like saturation magnetization is still a great challenge, as particles below 8 nm are readily oxidized to maghemite, and in larger particles there is always a degree of surface oxidation and a core/shell structure of magnetite/maghemite is formed.[4,5] The other advantage of magnetite over maghemite nanoparticles is the possibility of better tuning the magnetic properties of the specimen in the magnetite structure through substituting a wide range of divalent metals (Co, Mn, Zn, etc.)[6−10] for Fe^{2+}.

Various synthesis methods have been developed for obtaining iron oxide nanoparticles; however, thermal decomposition is currently considered the most advanced one for controlling the shape, size, and crystallinity of the particles.[11] Despite the fact that even one-nanometer[12] or sub-nanometer scale size-controlled[13] iron oxide nanoparticles have been successfully achieved, the problem of low saturation magnetization in the resultant particles in such robust size-controlled reports is still debatable. For some other inorganic nanoparticles,[14,15] the intrinsic properties for their use in different applications may only be determined or satisfied by controlling the size or shape. However, when considering magnetic nanoparticles' applications, not only addressing the morphological features, but also their magnetic properties must be tuned differently based on each application. Although narrow size distribution may be the necessary condition for several applications such as magnetic recording[16] or biomedical imaging,[17] it is not a sufficient condition either; for the former, magnetically hard nanoparticles are desirable, while for the latter, a very soft magnetic material (superparamagnetic) will be favored. Accordingly, following some decisive previous works,[18−20] many other researchers of diverse disciplines have extensively attempted to modify or improve the synthesis protocols to achieve higher simplicity, yield efficiency, cost effectiveness, or better tunability of magnetic properties.

Synthesis of iron oxide nanoparticles using thermal decomposition is usually performed by the decomposition of organometallic iron precursors in the presence of an organic surfactant and a high boiling point solvent. This is mostly performed either by first preparation of iron(III) oleate as the precursor or by directly using an organometallic iron source such as iron(0)-pentacarbonyl [$Fe(CO)_5$] or iron(III) acetylacetonate [$Fe(acac)_3$]; because of its high toxicity and volatility, $Fe(CO)_5$ is not commonly used.[21] Using iron(III) oleate imposes an extra step to the synthesis and increases the time and complexity; any change in the quality of the iron oleate may significantly affect the characteristics of the resultant particles.[22] It has been shown that choosing different iron sources to prepare the iron oleate precursor can significantly influence its properties,[23] which in turn can result in less reproducibility of the synthesis procedure. $Fe(acac)_3$, on the other hand, has been widely used with several different surfactants,[24,25] reducing agents,[26,27] and solvents.[18−20] Although iron oxide nanoparticles can be obtained in a one-pot synthesis when using $Fe(acac)_3$, to produce larger particles seed-mediated growth method is often needed.[18,28] Benzyl ether is one of the widely used solvent with $Fe(acac)_3$, but it has been shown that benzyl ether's susceptibility to oxidation in air can dramatically influence the resultant particles and therefore the reproducibility of the synthesis.[21] Dioctyl ether (DE) and 1-octadecene, although less than benzyl ether, are other common solvents that have been used in different studies with both $Fe(CO)_5$ and $Fe(acac)_3$.[8,19,23,29]

Saturation magnetization (M_s) is one of the most important intrinsic properties of iron oxide nanoparticles that, for almost all applications, is preferred to be enhanced close to the value of the bulk material. There are several works in the literature that have successfully addressed the morphology and M_s value of the particles simultaneously, but most reports are not very clear on their synthesis procedures. For instance, except for the works that are concerned about specific parameters (e.g., studying the effect of the surfactant/iron precursor ratio or the heating rate), in many cases the important parameters such as the amount of solvents and reducing agents, the ratio between these two and the surfactant, the stirring method (mechanically or magnetically), steps in the heating profile, and so forth, are not expressed in detail. This becomes more pronounced when the particles have been obtained in two steps, either using iron oleate as a precursor or the seed-mediated growth method. In addition, the majority of these studies have been reported under vacuum syntheses using the Schlenk line, which imposes more difficulties for researchers. Given the fact that iron oxide nanoparticles have found application in many different disciplines, the inherent complexity of the thermal decomposition method, and the quest for simpler and clearer procedures to obtain monodisperse magnetite nanoparticles with high M_s values; in this study, we have attempted to provide in detail steps on the preparation of single domain magnetite nanoparticles with M_s values nearly equal to the bulk material. Based on several successful one-pot synthesis reports in the literature, we first synthesized several iron oxide nanoparticles under different conditions (types of the solvent, reducing agent, heating profile, and stirring conditions) to obtain particles with an acceptable saturation magnetization and size distribution (data not shown). Based on these preliminary studies and confirmation of the reproducibility for the final sample (sample A1 in this study), in three stages, we studied the effect of three parameters on the intrinsic properties of the resulting particles as follows: (A) the ratio between the solvent and the sum of the surfactant and the reducing agent, (B) the ratio between the surfactant and the iron source for the optimized sample of group A, and (C) the introduction of a secondary reducing agent and varying the amount of the primary one again for the optimized sample of group A. In fact, here the goal was to examine the possibility of changing the particle sizes while preserving the high saturation magnetization by modulating the chemical ratios in the reaction. We found two different synthesis conditions for reaching high saturation magnetization through a relatively simple procedure, wherein the resultant particles were monodispersed with considerably different sizes. Except for the samples in group B, other samples also had relatively high M_s values but different morphological properties. A comprehensive structural and magnetic characterization of all the samples is provided for better understanding the diverse magnetic properties of the particles. Moreover, using a well-established protocol for ligand exchange in the particles prepared by thermal decomposition, their phase transfer to an aqueous medium is presented. The biocompatibility of a chosen sample through the 3-(4,5-dimethylthiazol-2-yl)-2,5-diphenyltetrazolium bromide (MTT) assay was also evaluated.

2. EXPERIMENTAL SECTION

2.1. Materials. All the chemicals were of analytical grade and used as received. Iron(III) acetylacetonate [$Fe(acac)_3$] 99.9%, oleylamine (Ol) 70%, DE 99%, oleic acid (OA) 90%,

https://doi.org/10.1021/acsomega.2c01136
ACS Omega 2022, 7, 15996−16012

toluene 99%, ethanol 99%, 2,3-dimercaptosuccinic acid (DMSA), dimethyl sulfoxide (DMSO), and MTT powder were purchased from Sigma-Aldrich. 1,2-Hexadecanediol (HD) 98% was purchased from TCI. The NIH/3T3 and U87 cell lines were purchased from the Korean Cell Line Bank (Seoul, Korea).

2.2. Synthesis Procedure. Three groups of iron oxide magnetic nanoparticles were synthesized. In the first group A, based on several previous studies,[18,30,31] the molar ratio between the surfactant (OA) and the iron complex was chosen as 3 = OA/Fe(acac)$_3$, and the molar ratio of the solvent (DE) with respect to the sum of OA and Ol (DE/OA + Ol) was varied. Hence, for this group, in a 100 mL three-neck round-bottom flask, 4 mmol Fe(acac)$_3$ was added to the mixture of 12 mmol OA and 36 mmol Ol. Then, 24, 36, and 48 mmol DE (DE/OA + Ol = 0.5, 0.75, and 1) as the solvent were added to the mixture for samples A1, A2, and A3, respectively. In group B, all the parameters used for sample A2 were kept the same except for increasing the ratio of OA to Fe(acac)$_3$ from 3 to OA/Fe(acac)$_3$ = 4, 5, and 6 in samples B1, B2, and B3, respectively. Finally, for group C, a fixed amount of HD (12 mmol) as a secondary reducing agent was added in reactions while preserving the OA and DE amounts similar to that in sample A2. However, the amount of Ol was varied in three steps; these were included as using C1 = 6, C2 = 12, and C3 = 24 mmol Ol in the reactions. In sample C3, the sum of HD and Ol moles was equal to that of Ol for sample A2 (36 mmol).

The heating profile in all the three groups was kept identical. To control the heating process, a ramping/profile control device Glas-Col 104A PL924K connected to a heating mantle (DAIHAN DHM.12111 90W) was used. After mixing all the reactants, under a flow of N_2 in the flask, the temperature was raised to 110 °C with a heating rate of 6 °C/min under magnetic stirring (750 rpm). The mixture was kept at this temperature for 60 min without the condenser to remove the residual moisture in the flask. Then, the condenser was connected, followed by raising the temperature to 185 °C at a rate of 3 °C/min. The temperature was maintained at 185 °C for 90 min to ensure the complete decomposition of the iron precursor. Subsequently, the reaction mixture was heated to 295 °C at the same rate (3 °C/min) and refluxed for 80 min. Next, the heating mantel was immediately removed, and the mixture was allowed to cool down to room temperature. All the steps were performed under the same stirring conditions. Upon reaching room temperature, the product was precipitated by adding ethanol and washed four times using a mixture of toluene/ethanol, 20/80, and by centrifugation (12,000 rpm, 15 min). The final products were then stored in toluene. To obtain the powder samples, in order to ensure the removal of any extra unbounded surfactant in the medium, each was additionally washed six more times using the same procedure. In the last washing step, the particles were separated using a permanent magnet and dried at 35 °C under N_2.

2.3. Characterization. The magnetic nanoparticle sizes and morphologies were characterized using a Transmission Electron Microscope (TEM), Tecnai G2 F30 S-Twin. For acquiring the images, samples were prepared by simply drop casting 10 μL of a diluted dispersion of the nanoparticles in toluene on a 200 mesh copper carbon support film CF200-CU. This method usually leads to clumps of nanoparticles upon drying, even if the particles are well-dispersed in the colloid without aggregation.[32] Several methods have been reported to create a monolayer sell-assembly of fine particles.[16,33] We additionally used the Langmuir−Blodgett method[34] for samples C2 and C3 to confirm that the observed clumps were in fact the result of the TEM sample preparation method and not aggregation in the particles. The nanoparticles' diameter and distribution were determined by measuring at least 800 particles using ImageJ software.

The X-ray diffraction (XRD) of powder samples was performed between 20 and 80 (2θ) degrees by using a Rigaku SmartLab X-ray diffractometer equipped with a copper X-ray tube and Cu Kα. Phase identification and whole pattern fitting were performed on the results using FullProf Suite and PDXL software of the XRD device. Using the line broadening originated from the small size of the crystallite and considering the instrumental broadening, crystallite sizes were estimated using the Scherrer equation (eq 1)[35,36] and compared with the crystallite size obtained by the Williamson−Hall method (eq 2)[37]

$$\left(D = \frac{K\lambda}{\beta \cos\theta}\right) \tag{1}$$

$$\beta \cos\theta = \frac{K\lambda}{D} + 4\varepsilon \sin\theta \tag{2}$$

In both equations, K is a numerical factor known as the crystallite shape factor and can be considered 0.94 for spherical nanoparticles with a cubic crystal structure,[38] λ is the wavelength of the radiation (1.5406 Å), and θ is the Bragg angle. However, β in the Scherrer equation is considered as the broadening only due to the size effect, but in Williamson−Hall as a contribution of the size and the strain in the lattice structure. In the Williamson−Hall plot ($\beta \cos\theta$ vs 4 $\sin\theta$), the y-intercept of the linear fit gives the crystallite size, and the slop indicates the strain ε. The lattice parameter for each sample was calculated using the Cohen's method, which is considered as one of the most accurate methods for calculating the lattice parameter from XRD data.[36,39]

The Raman spectra of powder samples at room temperature were collected using a HORIBA LabRAM HR Evolution unit with a 532 nm laser source. A Lorentzian function was used to fit/deconvolute all the spectra in the region between 100 and 900 cm^{-1}, according to previous work.[40] The Fourier transform infrared (FTIR) spectrum of the powder samples was also recorded using a Bruker Vertex 70v system between 4000 and 300 cm^{-1}. Thermogravimetric analysis (TGA) was conducted using the SHIMADZU TGA-50 system from room temperature to 600 °C at a 20 °C/min rate and under an argon atmosphere. The surfactant graft density (GD) of the particles was estimated based on TGA data and their first derivative (DTGA). The room temperature magnetization curve of the samples was measured using a vibrating sample magnetometer, 7404-S, Lake Shore Cryotronics, Inc. The magnetization values were calculated by subtracting the surfactant mass from the whole particle mass using the TGA data. This enables us to report the magnetization values of the magnetic cores. The effective anisotropy constant (K_{eff}) of the samples was estimated by employing the law of approach to saturation as

$$M = M_s\left(1 - \frac{a}{H} - \frac{b}{H^2}\right) + cH \tag{3}$$

where $b = \beta K_{eff}^2/\mu_0^2 M_s^2$ and for magnetic nanoparticles with uniaxial anisotropy, β is 4/15.[41]

https://doi.org/10.1021/acsomega.2c01136
ACS Omega 2022, 7, 15996−16012

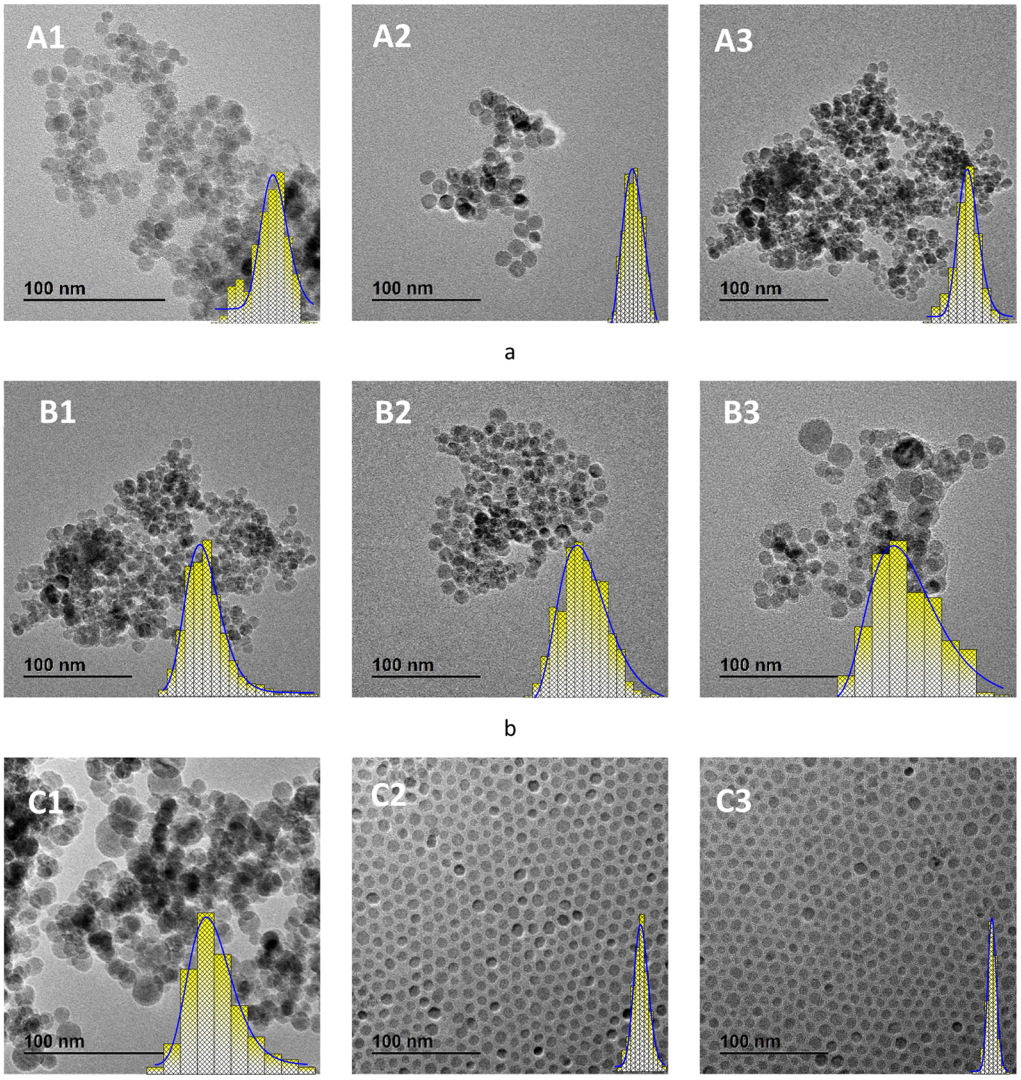

Figure 1. TEM images of samples of (a) group A, (b) group B, and (c) group C.

2.4. Phase Transfer from Toluene to Aqueous Medium. To disperse the particles in water, we utilized a facile and well-known protocol using DMSA.[42] Prior to the phase transfer procedure, the concentration of the particles in toluene was determined using a colorimetric method. Indeed, we determined the iron concentration in the dispersions and then converted the results to the particle concentration by supposing only magnetite particles in the sample. A colorimetric standard was first plotted using $FeCl_3{\cdot}6H_2O$ and $FeCl_2{\cdot}4H_2O$ (2:1, w/w). Briefly, various concentrations of Fe were prepared in a HCl solution, and 50 μL of each solution was transferred into a 96-well plate. Subsequently, 50 μL of 1% ammonium phosphate and 100 μL of 0.1 M potassium thiocyanate were added to the solution. After 5 min of the reaction, the absorbance of the solution was measured at 490 nm using a microplate reader (Varioskan LUX, 3020, Thermo Scientific). For each sample, toluene was first volatilized under a vacuum, and subsequently, the dried sample was dissolved in HCl and reacted with the reagents, employing the same procedures as in the standard samples. Finally, the iron content of each sample was calculated using the standard curve.

In brief, the typical procedure of the phase transfer protocol was as follows: 10 mg of DMSA was dissolved in 1 mL of DMSO and then the solution was added to a 1 mL dispersion of the particles in toluene with a concentration of 10 mg/mL (the concentration of the solid cores). The resulting mixture was then rotated at room temperature overnight to allow the ligand exchange. Then, particles were separated magnetically and washed several times with deionized water. The final product was stored in water and the pH was adjusted to ~7. The surface charge of the particles before and after surface modification was determined using the Zetasizer Nano ZSP, Malvern Instruments.

2.5. In Vitro Cellular Toxicity Evaluation (MTT Assay). An MTT assay was conducted to evaluate the cell viability and cytotoxicity induced by magnetic nanoparticles after surface modification. NIH/3T3 and U87 cell lines were seeded (1×10^4) into 96-well plates for 24 h and then magnetic nanoparticles from the known concentration stock were added to achieve the final concentrations of 5, 10, 15, 30, 60, 120, and 240 μM. The prepared serial concentrations were added to 96-well plates ($n = 3$) and incubated individually for 24, 48, and 72 h under optimum growth conditions. Then, the MTT solution (20 mL, 5 mg/mL) was added to each well and incubated at 37 °C for an additional 4 h. Absorbance at 570

https://doi.org/10.1021/acsomega.2c01136
ACS Omega 2022, 7, 15996−16012

Table 1. Summary of the Particles' Mean Diameter Obtained by TEM and Crystal Properties Estimated by XRD Patterns[a]

samples	mean diameter (TEM)	crystallite size (W−H)	crystallite size (Sch)	microstrain × 10^{-3}	lattice parameter	d-spacing (311)	synthesis parameters
A1	12.6 ± 1.6	11.65	12.27	0.64	0.8372	0.2524	0.5[b]
A2	13 ± 1	12.60	12.64	0.24	0.8375	0.2529	0.75[b]
A3	9.4 ± 1.1	8.15	8.4	0.49	0.8370	0.2528	1[b]
B1	10 ± 2.5	7.53	8.83	3.1	0.8399	0.2535	4[c]
B2	10.1 ± 2.6	7.70	8.18	1.14	0.8403	0.2537	5[c]
B3	11.8 ± 3.6	9.24	9.3	1.87	0.8420	0.2536	6[c]
C1	12.4 ± 3.4	10.59	11.15	1.55	0.8370	0.2530	6[d]
C2	9.3 ± 0.8	9.11	9.14	0.43	0.8369	0.2528	12[d]
C3	8.3 ± 0.5	6.1	6.23	1.72	0.8373	0.2524	24[d]

[a]All the sizes are presented in nanometer. [b]DE/OA + Ol ratio, in this group the ratio OA/$Fe(acac)_3$ was kept constant at 3. [c]OA/$Fe(acac)_3$ ratio, all other parameters were kept the same as in sample A2. [d]The Ol amount (mmol) and a fixed amount of HD = 12 mmol were used. Other parameters were kept the same as in A2.

nm was measured using a microplate reader (ELx800, BioTek, USA).

3. RESULTS AND DISCUSSION

3.1. Structural Properties and Phase Identification. In this study, the synthesis of iron oxide nanoparticles was evolved in three steps by studying the effects of (A) the molar ratio of the solvent with respect to the sum of the surfactant and the reducing agent, (B) the molar ratio of the surfactant with respect to the iron complex precursor, and (C) adding a secondary reducing agent in the reaction at the expense of decreasing the primary one, on the intrinsic properties of the resulting particles. In the first step, a widely used ratio between the surfactant and the iron complex [OA/$Fe(acac)_3$ = 3][18,30,31] was chosen. Then, we tried to find an optimal amount of the solvent to obtain monodisperse iron oxide magnetic nanoparticles with high saturation magnetization. Figure 1a shows the TEM images of samples A1, A2, and A3, wherein the molar ratio of the solvent was chosen as DE/OA + Ol = 0.5, 0.75, and 1, respectively. To estimate the mean particles' diameter, the histogram of each sample, obtained by measuring at least 800 particles in its TEM images, was fitted to a lognormal distribution function. With the ratios of 0.5 and 0.75, almost similar particle sizes were obtained (A1 = 12.6 ± 1.6 and A2 = 13 ± 1), but the latter resulted in lower particle size polydispersity (∼12.7 and 7.7%, respectively). By increasing the ratio to 1, the particle size decreased to 9.3 ± 1.1 in sample A3, but its polydispersity (11.8%) remained close to that of sample A1. Considering the polydispersity of less than 10% as monodisperse nanoparticles, sample A2 can be regarded as monodisperse; however, the other two samples also have relatively narrow size distributions. Here, the polydispersity values were obtained by dividing the standard deviation by the mean particle diameter of each sample and then multiplying by 100.

Based on these results for the group A, we chose sample A2 as the standard sample and increased the ratio of OA/$Fe(acac)_3$ from 3 to 4, 5, and 6 for sample B1, B2, and B3, respectively. Figure 1b presents the TEM images and histograms of this group. Surprisingly, the reaction for samples B1 and B2 resulted in nanoparticles with the same diameter ∼10 nm, which are 3 nm smaller than the standard sample A2. Although the mean diameter increased to 11.8 nm by a further increase in the molar ratio of OA/$Fe(acac)_3$ in sample B3, the average size still remained smaller than in sample A2. In all the samples from this group, the polydispersity increased dramatically. For example, in sample B3 it reached 31%, which is four times higher compared to sample A2. In the third group, we added a fixed amount of HD as an extra reducing agent to the reaction condition of sample A2 and varied the amount of Ol in three steps. As shown in the TEM images in Figure 1c, in sample C1, the mean particle size (12.4 ± 3.4 nm) remained almost the same as in sample A2, but it resulted in a very high polydispersity of ∼28%. By further increasing the amount of Ol in the reactions to 12 and 24 mmol, the particle diameters were reduced considerably to 9.1 and 8.3 nm for samples C2 and C3, respectively. However, the resultant particles were monodispersed with C1 = 8% and C3 = 6% polydispersity. The structural properties and synthesis parameters of all the samples are listed in Table 1.

Usually, the LaMer mechanism[43] is utilized to understand the nucleation and growth of the particles in thermal decomposition synthesis. According to this mechanism, nucleation and growth in the course of the reaction happen at three points: a fast increase in the number of the monomers (or growth species) as the smallest subunit of the bulk crystal in the solution, burst nucleation, which decreases the concentration of the monomers dramatically, and finally the growth of the formed nuclei by the diffusion of the monomers.[44] In group A, the molar ratio of the solvent with respect to the other reagents was increased in three steps. Although the size of the particles for the first two ratios did not show a notable change, it decreased for the highest ratio (sample A3). Based on the LaMer theory, because the diffusion distance for the growth species is longer for a higher amount of the solvent, it results in a lower mass transfer in the solution for reaching the nuclei. Therefore, for the same duration of the reaction, smaller particles may be formed. Such results have also been observed in previous reports.[30,45]

In several studies, decreasing,[31,46−48] increasing,[19,49−51] or even nonmonotonous behaviors[47,52] in the particle sizes have been reported by increasing the molar ratio of the surfactant to the iron precursor. Such trends observed in our samples can be explained and understood based on the changes that have probably happened in the reaction kinetics due to the change in amount of the surfactant. It has been shown that the decomposition temperature of $Fe(acac)_3$ can be considerably changed in the presence of surfactants, depending on either the surfactant type or the ratio between the surfactant and $Fe(acac)_3$.[24,53] Meanwhile, the critical parameter in thermal decomposition for obtaining monodisperse nanoparticles with accurate control over the size and crystallinity is the separation

https://doi.org/10.1021/acsomega.2c01136
ACS Omega 2022, 7, 15996−16012

between the nucleation and growth stages.[12,54,55] This separation can be achieved if either these two stages happen at two distinct temperatures or when the rate of nucleation and growth are sufficiently different. However, even if the temperature of these two stages is different, at some points there may be an overlap between them. Hence, the rate at which these two reactions progress plays a more important role.[56] The amount of the surfactant in the reaction can affect both the nucleation temperature (as a result of the change in the decomposition temperature) and the growth rate (as a result of the formation of more stable nuclei).[31,47] In all our reactions, the heating profile, including the heating rates and the constant temperatures at which the reaction was held for a certain time, was a constant parameter. It is speculated that because of the possible changes in the decomposition temperature and the nucleation and growth rates induced by increasing the amount of the surfactant, not only the particle sizes in group B decreased but also their polydispersity increased significantly. However, in group C, when HD was added to the reaction and the Ol was varied, at first (sample C1), no notable change in size but a considerable change in polydispersity compared to sample A2 was observed. In fact, we added HD as a widely used reducing agent in the reactions of group C to examine whether the coexistence of two reducing agents (Ol and HD) can also lead to the formation of particles with a narrow size distribution and high saturation magnetization. However, because HD reactivity is less than Ol (in other words, Ol is a stronger reducing agent than HD),[27,57] it seems that the molar sum of these two in the reaction of sample C1 did not sufficiently keep the kinetics of the reaction as in sample A2 to obtain particles with a lower polydispersity. However, the saturation magnetization in this sample was relatively high (see the magnetic characterization results). It has also been proven that Ol can have dual functionality, acting as both a reducing agent and a surfactant for stabilization.[27] In samples C2 and C3, by increasing the amount of the Ol, not only the sum of the molar ratio of reducing agents with respect to the other chemicals was increased but also Ol may have acted as a surfactant in the reaction (the hypothesis that was confirmed by the FTIR results of sample C3). Both increasing the reduction rate and the presence of ligands with amine function groups preferentially lead to the production of smaller particles.[47,57] Although we inferred the observed trends in our samples' size and polydispersity based on the changes that can happen in the kinetics of the reactions, for an in-depth insight into the effect of different reagent amounts, in situ studies during the reaction for understanding the nucleation and growth stages are needed.

As a final remark, we would like to highlight the important role of sample preparation for TEM analysis. As it was mentioned in the experimental section, all the TEM samples were prepared by simple drop casting a diluted sample on a TEM grid. However, because clumps of nanoparticles appeared in all the images, in order to verify whether the clumps were the result of particle aggregation or the TEM sample preparation method, the TEM analyses of samples C2 and C3 were repeated. However, this time the TEM samples were prepared using the Langmuir–Blodgett method as a standard and well-known method which can result in a monolayer of self-assembled nanoparticles.[34] Figure 2 clearly shows the long-range self-assembly of sample C3 prepared by using Langmuir–Blodgett versus its image obtained from simple drop casting. Therefore, it can be concluded that there is no or little actual particle aggregation in samples, and the clumps in TEM images are the result of the method chosen to disperse the particles onto the TEM grids.

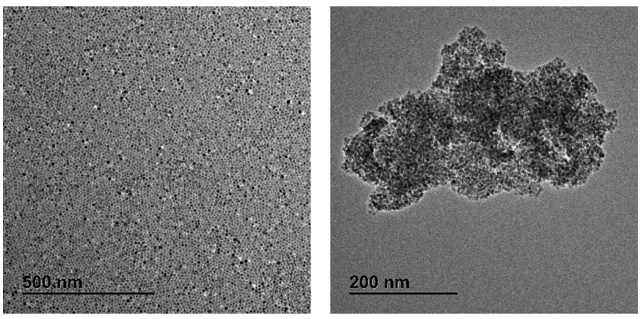

Figure 2. TEM images of sample C3 when the particles were dispersed onto the TEM grid by the (a) Langmuir–Blodgett method and (b) simple drop casting.

The XRD patterns of the powder samples were recorded to identify their structural phases. A typical whole pattern fitting (sample A1) to the pseudo-Voigt function and the XRD patterns of all the samples are presented in Figure 3. The peak positions and their relative intensities in all the samples of group A are in very good agreement with the cubic inverse spinel structure of pure magnetite (JCPDS no. 88-0315, space group: $Fd\bar{3}m$). The lattice parameter for the samples (Table 1) in this group were also in very good agreement with the corresponding reference card (8.375 Å). The XRD patterns in the samples of group B are best matched with the magnetite reference card JCPDS no. 72-2303 with a lattice parameter of 8.400 Å. The relative intensities and positions of the peaks in group C are also very well matched with the same JCPDC reference card as for group A. The *d*-spacing calculated for the crystal planes in all the samples was also in excellent agreement with the values reported in the reference cards. For instance, the values for the (311) plane are 2.52516 and 2.53270 Å in the standard cards 88-0315 and 72-2303, respectively (see Table 1 for comparison).

In all the XRD patterns, a clear line broadening can be observed, which results from size effects. This peak broadening can be utilized to estimate the mean crystallite size and the lattice strain in particles due to crystal imperfection and distortion. For the Scherrer equation, the mean crystallite sizes were obtained using the most intense peak (311), while for the Williamson–Hall plot, all the peaks were used. The detailed results are presented in Table 1. The crystallite sizes are almost the same or slightly smaller than the particle sizes, indicating that each particle consists of a single crystal.

In order to further investigate the crystal structure of the samples, Raman spectroscopy was conducted for all the samples. It has been shown that magnetite nanoparticles undergo a phase transition under laser radiation due to induced temperature elevation.[58,59] Magnetite transfers to maghemite at 200 °C and then hematite at 450 °C in an air atmosphere.[7,60] Raman spectroscopy was conducted under different laser powers and only by using 1% power of the laser beam (0.35 mW) an acceptable signal with a minor phase transition could be obtained. A typical phase transition of the samples under different laser irradiation powers is presented in Figure 4. By increasing the source power, the peak at around 668–675 cm^{-1}, which is the characteristic Raman shift for magnetite, first moved to a higher band around 720 cm^{-1}

https://doi.org/10.1021/acsomega.2c01136
ACS Omega 2022, 7, 15996–16012

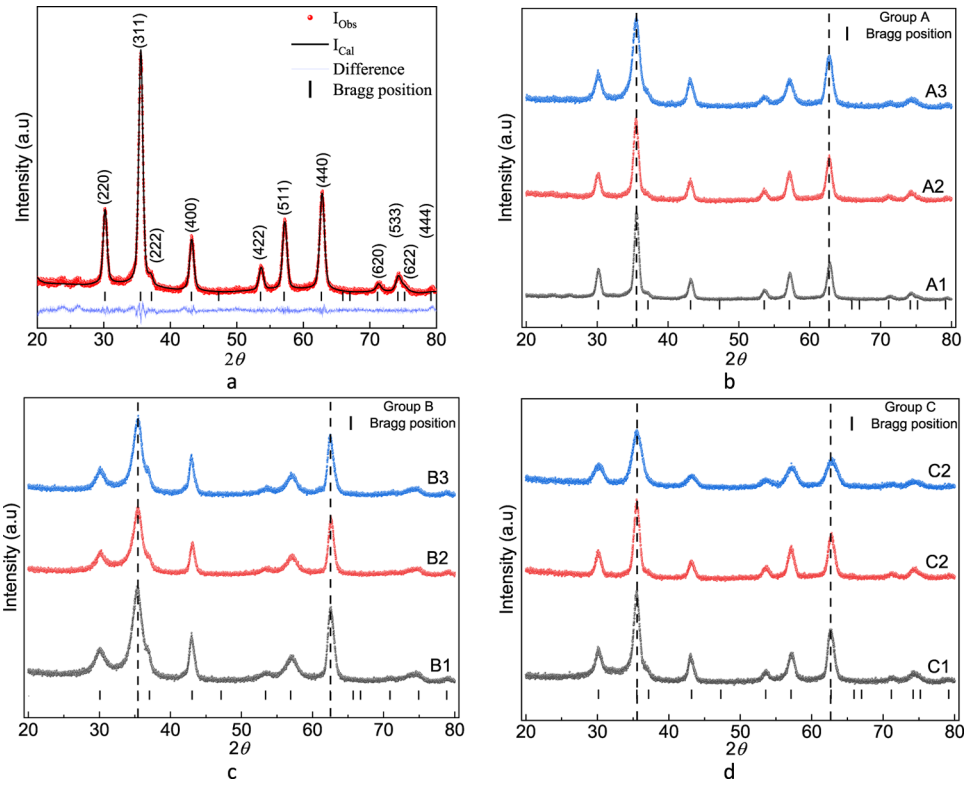

Figure 3. (a) Typical XRD whole pattern fitting and the (b−d) XRD patterns of the samples with respective Bragg positions from the reference cards.

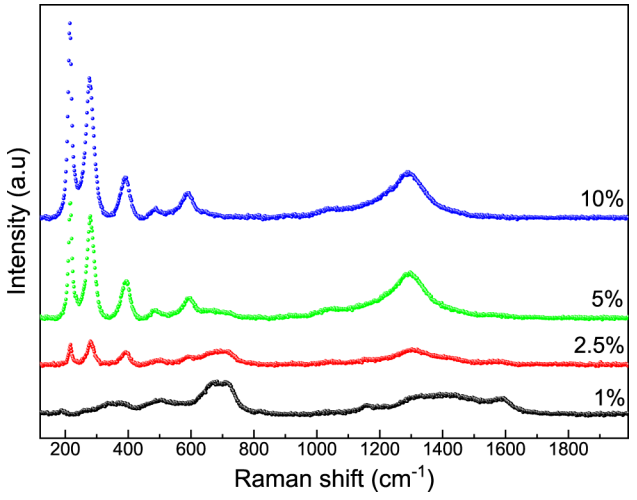

Figure 4. Raman spectra of sample A2 under different laser radiation powers.

(maghemite), then disappeared, and the peaks related to the hematite structure started to grow. At 3.5 mW, the spectrum suggests the complete transition of the sample to hematite. The lines observed at 214, 274, 390, 489, and 585 cm^{-1} are characteristic of the hematite $D^6_{3d}(R\bar{3}c)$space group.[58] The phase transition has especially been observed for the 532 nm laser source, and the 632 nm line is mostly recommended to be used for magnetite samples.[40] Unfortunately, the 532 nm laser was the only available source for us at the moment.

The Raman spectra of all the powder samples recorded at 0.35 mW power are shown in Figure 5. To analyze the spectra, they were all fitted by the Lorentzian function, and a typical fit is presented in Figure 5a. Based on the fitting results, there were at least five lines that can be attributed to the magnetite and/or maghemite structure. The corresponding Raman shifts are listed in Table S1 of the Supporting Information. These lines that were observed in the same regions for all the samples are lines at around 180−190, 338−348, 504−509, 668−675, and 719−721 cm^{-1}. Among these, the peaks between 180−190 and 668−675 cm^{-1} are specifically the characteristic signature of magnetite, and the peaks at around 720 cm^{-1} are attributed to the presence of maghemite,[61,62] which is most probably due to the oxidation of Fe^{2+} to Fe^{3+} on the surface of samples under the laser radiation.[63] However, other lines have been observed in the spectra of both maghemite and magnetite nanoparticles in different studies.[58,61,63,64] The region at 850−1750 cm^{-1} of the spectra is known as the fingerprint region of the organic molecules. The bands at around 1600 cm^{-1} and in the region between 1300 and 1400 cm^{-1}, which clearly appeared in all the samples, are, respectively, attributed to the asymmetric and symmetric vibrations of the carboxylate group bonded to the surface of the particles.[63] This result, along with the following FTIR data, could confirm the covalently bonded OA molecules on the surface of the particles.

The FTIR analysis on powder samples (Figure 6) also confirmed the magnetite phase in all the samples. Bulk magnetite has two characteristic absorbance bands at around 570 and 375 cm^{-1}, originating from the Fe−O vibration modes of the bonds at tetrahedral and octahedral sites in the spinel structure.[65,66] In many studies for magnetite nanoparticles, the absorption band at around 570 cm^{-1} has been observed to split into two bands or a band shifted to higher wavenumbers with a shoulder.[66−72] Similarly, in our samples, this band was shifted to higher wavenumbers, as 570 to 585, 579, and 584 cm^{-1} with a shoulder at around 626, 625, and 628 cm^{-1} for groups A, B,

https://doi.org/10.1021/acsomega.2c01136
ACS Omega 2022, 7, 15996−16012

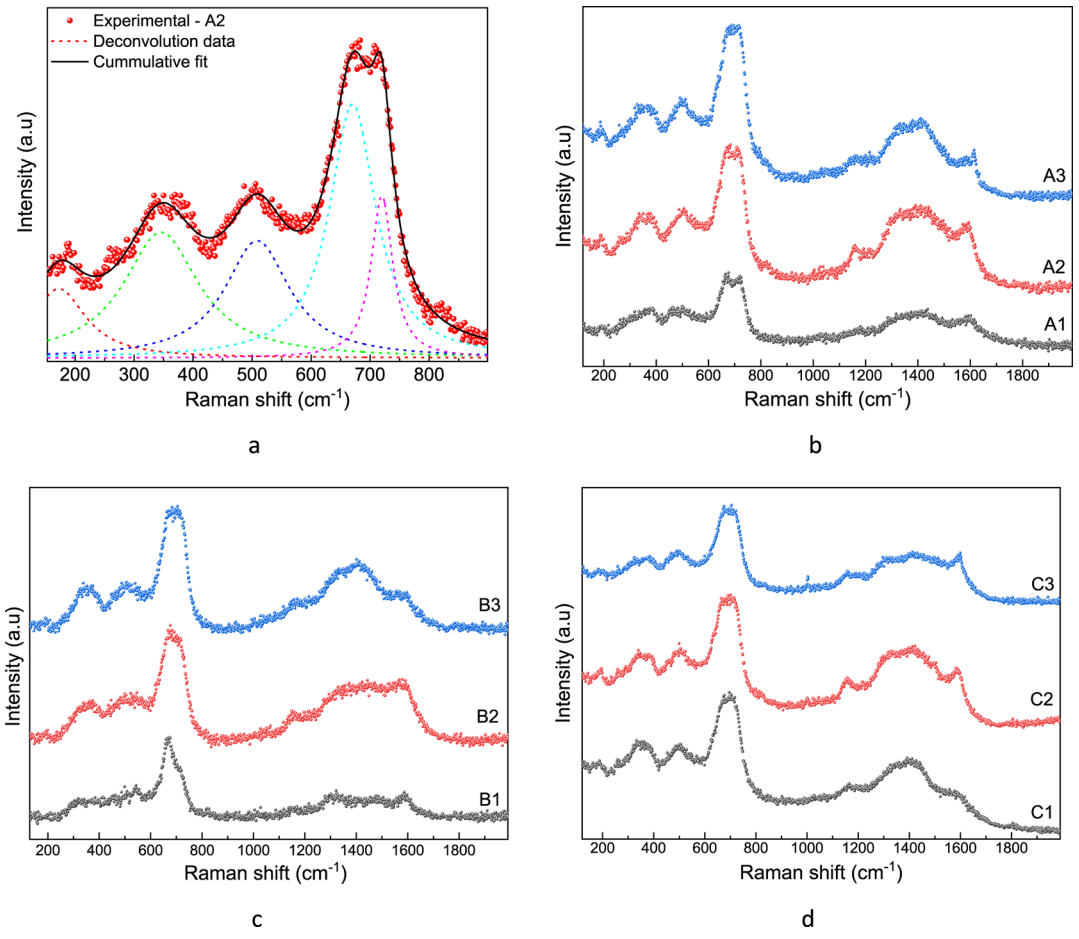

Figure 5. (a) Typical deconvolution of the Raman spectrum for sample A2 and the (b–d) Raman spectra of powder samples recorded at 0.35 mW laser power.

and C, respectively. The shift in band 370 cm^{-1} was observed to happen at 394, 390, 388 for the groups A, B, and C, respectively. This behavior can be related to size effects at the nanoscale, where many symmetry degeneration, broken bonds, and defects happen on the surface of the particles, leading to the rearrangement of nonlocalized electrons.[71,73,74] Although these peaks are also close to those observed for the maghemite structure, based on the values obtained for the lattice parameters from the XRD data and the magnetic measurements, presented in the following sections, it is hard to clearly assign the observed spectra to maghemite. In addition to the broken symmetries on the surface of the particles, surface oxidation, either as a nearly unavoidable phenomenon in fine magnetite nanoparticles[5,6,20,75,76] or due to the partial formation of maghemite because of the interaction between the Fe atoms and the carboxylate groups on the surface at high pressure conditions when preparing the KBr plates[63] may also happen. This can be another reason for the peak shifts and splitting. Moreover, maghemite shows several absorbance bands in the range of 500–700 cm^{-1},[5,77,78] which are absent in our samples.

The absorbance bands of the organic surfactant on the surface of the particles were clearly observed at higher wavenumbers. It has been shown in several studies[27,79–82] that Ol can act as both a surfactant and a reducing agent. Because in all our synthesis batches, both Ol and OA are present and the absorbance bands of OA and Ol capped nanoparticles are very similar,[66,69,82] great caution should be exercised in assigning the peaks to each vibration mode. The FTIR spectrum of pure OA has two peaks at 2924 and 2854 cm^{-1}, which correspond to asymmetric and symmetric stretching of CH_2. These peaks, after chemisorption of OA molecules on the surface of the particles, are slightly shifted to lower wavenumbers.[69] The occurrence of these two shifted peaks in all the samples can clearly show that OA molecules are coordinated with Fe atoms on the surface of the particles. The absorption of OA on the surface of the nanoparticles through the interaction between the carboxylate group and the Fe atoms and also its coordination type can be estimated from the region 1700–1300 cm^{-1} of the FTIR spectra.[22,83,84] Three different coordination structures, namely unidentate, chelating (bidentate), and bridging complexes, have been proposed for binding the carboxylate group with the metal atom on the surface of particles. In a unidentate structure, only one of the oxygen atoms in the carboxylate binds with one metal atom on the surface, while in the bidentate type, both oxygen atoms bind with a single metal on the surface. For a bridging complex, there are two bonds between the carboxylate and the surface of the particles, that is, each oxygen atom is bound to a metal atom.[84]

It has been reported that, in a metal carboxylate structure, a peak appears between 1650 and 1510 cm^{-1} for the asymmetric vibration and for the symmetric vibration in the range of 1400–1280 cm^{-1}.[22,85] However, the presence of two different coordination modes can result in a band splitting and the appearance of extra peaks, related to the interaction of the

https://doi.org/10.1021/acsomega.2c01136
ACS Omega 2022, 7, 15996–16012

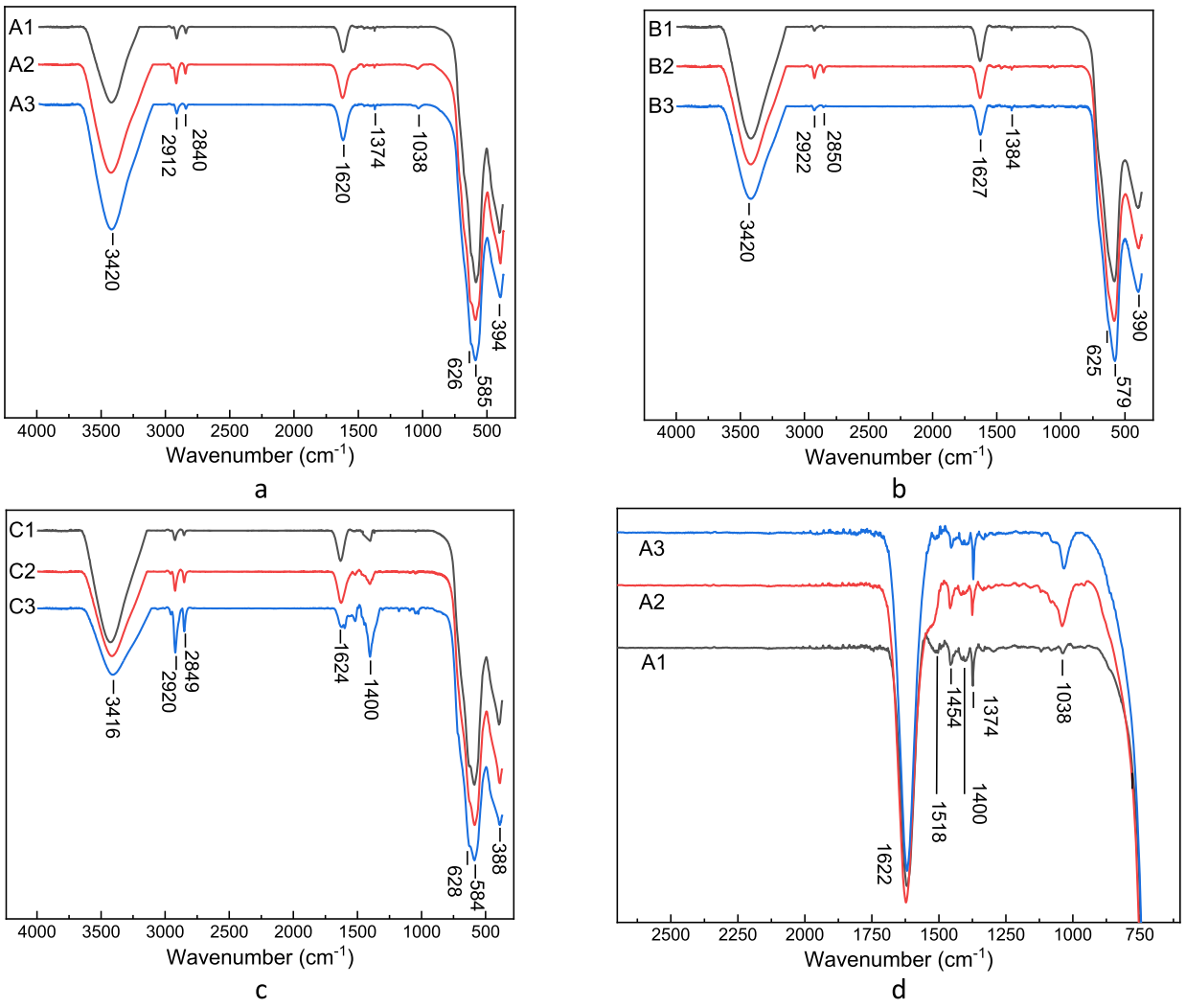

Figure 6. (a–c) FTIR spectra of powder samples and the (d) magnification of the region 1700–1300 cm^{-1} for samples in group A.

carboxylate headgroup with the iron atoms, in the region of 1700–1300 cm^{-1}.[13,22,86–88] The coordination type can be estimated by using the separation between the asymmetric and symmetric vibrations in this region [$\Delta = \nu_{as}(COO^-) - \nu_s(COO^-)$]. A unidentate structure is expected when $\Delta > 200$ cm^{-1}, whereas $\Delta < 110$ cm^{-1} the binding is anticipated to be a bidentate ligand, and finally for values between 140 and 200 cm^{-1}, a bridging complex is proposed. Although this method, as an empirical method, may not be sometimes very precise, especially for aqueous solutions,[89] it can provide a good estimation as it has widely been used in the literature.[69,90] Particularly, it can be useful for relative comparison of the changes that can happen among samples with the same composition but prepared in different conditions.

Although in some of the samples, the bands in these regions had very low intensities, by careful inspection of the region, they could clearly be identified. Figure 6d shows a typical magnification of the region for samples in group A, and Table S2 in the Supporting Information presents the bands identified in this region for each sample. As can be seen, except for sample B3, at least four peaks in this region can be identified, where they can be attributed to asymmetric and symmetric vibrations of $\nu_{as,s}(COO^-)$.[86] Based on these speculation, the separation (Δ) between the asymmetric and symmetric vibrations demonstrates either the bidentate ($\Delta < 90$ cm^{-1}) or bridging binding ($120 < \Delta < 180$ cm^{-1}) structure between the carboxylate group and the Fe atoms of the samples. The band at around 1622 cm^{-1}, which is relatively strong in all our samples, has been assigned very differently in previous studies.[91] For example, it has been assigned to $\nu_{as}(COO^-)$[69,92,93] or N–H bending,[27,79,82,94] however, this band in our samples cannot simply be assigned to either of these bonds. Especially, because this and a very broad band at around 3420 (which may also be a result of N–H bending[95–97]) can be the result of O–H stretching of observed water. Metal–organic structures can contain adsorbed water.[91] This is more probable in the samples of the present study because for preparing the powder samples, the particles dispersed in toluene were washed several times with an excess of ethanol.

Lastly, in all the samples, except for sample C3, due to the absence of the characteristic peaks of pure OA (1710 cm^{-1}) and Ol (1593 and 3300 cm^{-1}), it can be concluded that there is no trace of free OA or Ol on the surface of the particles.[79] In sample C3, a weak peak appeared at 1600 cm^{-1}, which is probably due to physisorption (van der Waals interactions) of the Ol molecules on the surface of the particles. The presence of an extra reducing agent in group C and the excess of Ol for synthesizing sample C3 could probably be the reason for this observation. Physisorption moieties can form more than one

https://doi.org/10.1021/acsomega.2c01136
ACS Omega 2022, 7, 15996–16012

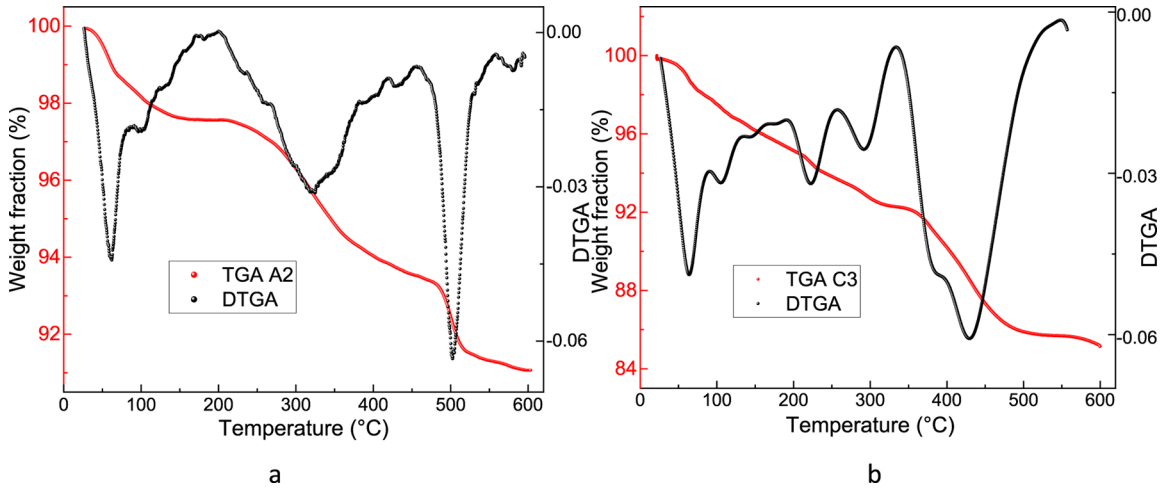

Figure 7. TGA and DTGA of powder samples (a) A2 and (b) C3.

layer or be absorbed on top of the chemisorbed molecules, which usually form a monolayer on the surface.[95] This result was also supported by the TGA of the sample C3.

3.2. Thermogravimetric Analysis. Figure 7a shows a typical TGA/DTGA (sample A2) obtained from room temperature up to 600 °C with a heating rate of 20 °C/min under an argon atmosphere. This relatively fast heating rate was chosen because the aim here was only to estimate the amount of the organic matter absorbed on the particles and not an in-depth TGA study, which may provide information about the surfactant type or mono-/bilayer coating too.[98,99] However, even with this high rate, there was a clear difference between the TGA graph of sample C3 (Figure 7b) and the other samples. The FTIR of this sample was also different and showed an extra peak related to Ol, where it may be either because of the physisorption of the Ol on the surface of the particles or due to the formation of a secondary layer on top of the OA molecules. In general, the TGA of all the samples (Figure S1 in Supporting Information) were very similar to the typical curves of OA-coated iron oxide nanoparticles obtained under an inert gas in several previous studies.[31,100,101] Based on the DTGA curves, for all the samples there was a sharp but small weight loss up to temperatures of around 100 °C, which is due to evaporation of the absorbed water or the residual of the solvent in the powder samples. The weight losses in other steps are related to the desorption and decomposition of the organic matter from the surface of the particles.[30] The total weight loss percentage values of the samples are presented in Table 2.

The weight loss obtained by the TGA can be used to estimate the GD of the organic molecules on the surface of the nanoparticles (the number of molecules per unit surface area). By assuming a perfect sphere shape for the particles and a monolayer of chemisorbed OA on their surface, the GD can be estimated as follows[100]

$$\mathrm{GD} = \frac{\rho V(w_i - w_f)}{w_f S M_w} N_A \quad (4)$$

where ρ, V, and S are the density, average volume, and average surface area of the particles, respectively. M_w is the molecular weight of OA (282.46 g/mol) and N_A is the Avogadro's number. The density of the particles was assumed to be 5.18 g/cm^3 (magnetite). Finally, w_i and w_f are the weights of the sample after the first and last peaks of the DTGA curves (the weight loss before the first peak should not be considered because it is related to the absorbed water), respectively. Based on these assumptions, values of between 0.7 and 2.1 molecules/nm^2 were estimated for the samples. Although this method provides a rough estimation of the amount of surfactant grafted onto the particles, it can be an easy but effective way to compare samples prepared in different conditions. These results are also in good agreement with the FTIR results by comparing the intensities of the bands at around 2920 and 2850 cm^{-1}, which are the characteristic bands for bonding the surfactant on the surface of the particles. Clearly, these bands are more intense in samples with higher GD. However, it should be noted that the intensities can also be directly related to the particle size, where particles with the largest surface/volume ratio may generate signals with a higher intensity of the coordinated surface molecules.[102] This effect can be obviously seen for samples A2 and C3, which both have almost the same GD but different sizes (13 and 8.3 nm, respectively). Interestingly, among the three groups, the GD was minimum in group B, where the OA/Fe(acac)$_3$ ratios were increased while keeping the other parameters constant, as in sample A2. In both groups A and C the OA/Fe(acac)$_3$ ratio was kept equal to 3 and almost a similar value around 2 molecules/nm^{-2} was obtained.

Table 2. Summary of the TGA, Estimated GD, Magnetic Diameter, Saturation Magnetization, and Effective Anisotropy Constant of All the Samples

	total TGA weight loss (%)	GD (molecule/nm^{-2})	magnetic diameter (D_{mag})	M_s (emu/g)	K_{eff} (10^4erg/cm^3)
A1	7.6	1.5 ± 0.4	10.69	67	20.4 ± 4
A2	9	1.9 ± 0.3	11.14	80	18.7 ± 2
A3	8.9	1.7 ± 0.4	9.34	63	31.7 ± 4.2
B1	6	0.7 ± 0.3	9.79	41	29.7 ± 4.1
B2	7.8	1.1 ± 0.8	9.45	50	30 ± 3
B3	5.3	0.9 ± 0.6	9.97	45	27.7 ± 4.5
C1	9.5	1.8 ± 0.9	10.74	72	29.7 ± 5
C2	10.2	1.7 ± 0.3	9.6	78	21.3 ± 2.2
C3	14.9	2.1 ± 0.3	8.13	65	31 ± 3.5

3.3. Magnetic Characterization. The room temperature magnetization curves of the powder samples at applied

https://doi.org/10.1021/acsomega.2c01136
ACS Omega 2022, 7, 15996−16012

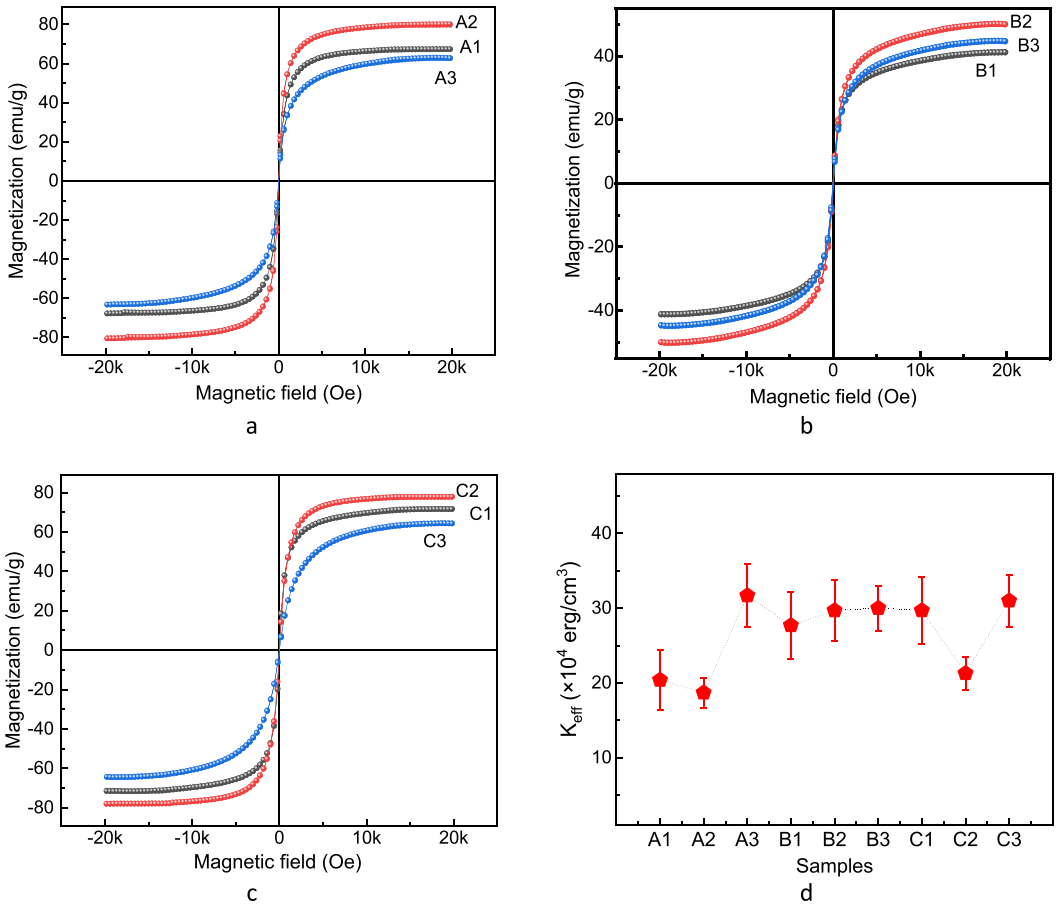

Figure 8. (a–c) Room temperature magnetization and (d) estimated effective anisotropy constant of all the samples.

magnetic fields of up to 2T are presented in Figure 8. All the samples were almost saturated at this field and showed no remanence and coercivity within our experimental setup, confirming their superparamagnetic state. This was expected based on their small sizes. The critical size for magnetite nanoparticles to be in a single domain state has been estimated at 49 nm.[103] Samples in group B, wherein the ratio of OA/$Fe(acac)_3$ was increased compared to the rest of samples, showed the lowest saturation magnetization. Their M_s values are in the range of typical values (30–50 emu/g) reported for nanosized iron oxide particles, even with very high-quality size and shape properties in several previous studies obtained by the thermal decomposition method.[12,13,20,49,104,105] It is well-known that the M_s values in iron oxide nanoparticles are much lower than their bulk counterparts (86 and 76 emu/g for magnetite and maghemite at room temperature, respectively[102,106]) and usually decrease with size.[49,107] However, iron oxide nanoparticles with small sizes have also been synthesized, which have shown M_s values equal or close to those of bulk magnetite.[8,18,28,106] Although the maximum difference between the largest and the smallest average sizes among the samples of the present study was about 5 nm, they showed very diverse magnetic properties. For example, while having different mean diameters, the M_s values of samples A2 (13 nm), 80 emu/g, and C2 (9.1 nm), 78 emu/g, were very similar and are among the highest values reported in the literature for iron oxide nanoparticles. On the other hand, samples B3 (11.8 nm) and C1 (12.4 nm) had very close average sizes, but a significantly different saturation magnetization (44 and 72 emu/g, respectively). Another noticeable result was related to the M_s value of the sample C3 (65 emu/g), as the smallest sample (8.3 nm), which is comparable to the saturation magnetization of sample A1 (12.6 nm).

It is widely accepted that the saturation magnetization of fine particles with any certain composition is directly governed by their size, but there are reports in the literature that even particles with a 4 nm size have shown values almost equal to their bulk counterparts.[18] Therefore, simply relating the size to saturation magnetization may not be appropriate, as it is evident in our samples too. For example, C3, with the smallest mean diameter, showed a significantly higher M_s value compared to sample B3. Because the first and probably the most important factor in determining the magnetic properties of nanoparticles is the synthesis method/condition, first of all, we would like to emphasize on the differences in synthesis conditions of the three groups. Particularly, the role of the surfactant as a determinant parameter, which can directly influence a variety of intrinsic properties of the resultant particles including size, their polydispersity, and magnetic properties. In groups A and C, the surfactant to organometallic precursor ratio was constant ($OA/Fe(acac)_3 = 3$), while it was increased to 4, 5, and 6 for samples B1–B3, respectively. In addition to its effect on the size and polydispersity of the particles, it resulted in a lower GD in the samples of group B. There are several studies highlighting the direct effect of surfactant interaction/bonding with the surface of particles on their magnetic properties.[108] The presence of covalently bonded OA on the surface of the particles not only reduces

https://doi.org/10.1021/acsomega.2c01136
ACS Omega 2022, 7, 15996–16012

the surface spine disorder significantly but also can result in highly crystalline particles with saturation magnetization close to bulk magnetite.[109] Moreover, such particles have proven to perverse the high magnetization even after ligand exchange or surface passivation.[110] Therefore, although FTIR analyses clearly showed the surfactant bonding in all our samples, the lower GD of OA in group B is in line with the reduced magnetization of these samples.

Another point that can also explain the diverse M_s values observed among our samples is their crystalline quality. Recalling the XRD results, more careful inspection of the patterns obviously shows that samples such as A1, A2, or C2 with very well-defined peaks have a higher degree of crystallinity. The agreement between the crystallite sizes estimated based on the XRD patterns and the mean diameters obtained from TEM images in samples with higher saturation magnetization can also indicate that the crystal structure of magnetite has been maintained up to the boundaries of the particles. However, one should keep in mind that the crystallite extended up to the boundaries or high surfactant GD may not necessarily lead to very high saturation magnetizations (close to bulk values) in nanosize particles. This is of particular relevance in particles prepared using the thermal decomposition method, where the antiphase boundaries (APBs) are vastly prevalent even among monodisperse particles.[105] APBs are defects that have been observed and studied in different nanostructures through microscopy[105] or simulation[111] work. They are considered one of the main reasons for reducing spin polarization.[105,111−113] For example, these defects may impose such a lattice vector shift in the atomic structure of the magnetite that the 90° Fe_B-O-Fe_B bonds in octahedral sites increase to higher angles, even higher than the angle between iron atoms in tetrahedral and octahedral sites (Fe_A-O-Fe_B), 125°; this in turn can alert the ferromagnetic superexchange interaction to the antiferromagnetic interaction on either side of the defect boundaries.[105,111] For each sample, we inspected several particles in their TEM images, where acceptable resolution and higher magnification images could be obtained. Using Gatan Microscopy Suite Software of the TEM device, we applied a fast Fourier transform (FFT) filter followed by an inverse FFT after masking the respective plan reflection to enhance the visualization of the crystal lattices. Although at first sight the crystal periodicity is maintained across the entire volume of the particles (at least for the visible crystal planes), after applying the FFT filters, only in samples A2 and C2 no or very little trace of lattice deformation or dislocation appeared (Figures 9a and S2 in the Supporting Information). In all the other samples, even in the highly monodisperse sample C3, considerable misfit dislocations, most probably due to the interfacial strain and defects in the crystal structure, were observed (Figure 9b). Nearly all of these dislocations were detected in the (111), (220), and (440) planes, especially for particles with lower saturation magnetizations among samples.

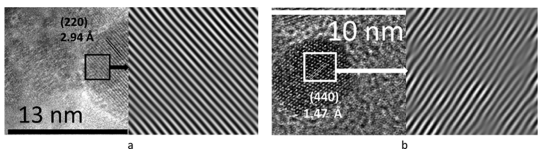

Figure 9. TEM image and the result of the FFT filters on a particle from samples (a) A2 and (b) C3.

Although the APBs were not quantitatively determined, their prevalence was qualitatively matched with the microstrain (estimated by XRD results) in the samples, where the sample A2/B2 with the highest/lowest saturation magnetization had the lowest/highest strain and ABPs. In addition, the *d*-spacing values obtained using the analysis of TEM images by FFT filters were in excellent agreement with those estimated by the XRD patterns.

The possibility of the presence of a magnetically dead outer layer in the particles was also examined by estimating the effective magnetic size of the samples using the low magnetic field region of the magnetization curves (Table 2). The magnetic size in this method can be obtained as[1]

$$D_{mag} = \left(\frac{18k_BT}{\pi M_s M_{sb}}\chi_i\right)^{1/3} \quad (5)$$

where χ_i is the initial susceptibility and can be deduced from the low field region of the magnetization curve, M_s is the saturation magnetization of the particles, and M_{sb} is the saturation magnetization value of the bulk material (in this case, magnetite). This method has been widely used in the literature for estimating the mean magnetic volume (or diameter). However, because it uses the low field part of the magnetization curve (initial susceptibility) and in this region for single domain particles, the main contribution is related to the largest particles, it should be interpreted as an estimation of the upper limit of the magnetic sizes and not the mean size.[114] Having this in mind and considering the standard deviations obtained from TEM images (Table 1), one can clearly conclude that the possibility of the existence of a dead layer in samples from group B is higher compared to the other samples. However, based on the sizes obtained by the TEM images, the magnetization curves, and crystallite sizes by XRD that are not very different from TEM sizes, we believe, in general, that the origin of the reduced magnetization in the samples is mainly due to the presence of the ABPs in the particles. In fact, the higher GD of OA has led to better crystallization and enhanced the spin polarization in the surface of the particles.

In addition to the effect on M_s values, the presence of microstrain and APBs in the particles can significantly influence the way that their magnetization curve approaches saturation. This effect has been empirically expressed in the law of approach to saturation magnetization and is widely used to estimate the effective anisotropy constant.[41] It is well-known that upon decreasing the size, the effective anisotropy can increase significantly.[115] However, the presence of microstrain can result in higher anisotropy constants in larger particles too.[116] The direct and significant effects of strain and lattice deformation on the effective anisotropy of the samples were also observed (Table 2 and Figure 8d). For instance, samples C2 and A3 have almost the same mean diameter, but the effective anisotropy constant in C2 was smaller than in A3. On the other hand, this value was almost the same as the value estimated for A2, while A2 has a larger mean diameter than C2. Interestingly, the effective anisotropy constant estimated for sample A2 was exactly the same as the effective anisotropy for bulk magnetite 18.7×10^4 erg/cm^3 (calculated based on the first- and second-order magnetocrystalline anisotropy constants of bulk magnetite[117]). This can indicate that in sample A2, which had the highest M_s value, the contribution of other sources of anisotropy (surface or induced by strain) compared to magnetocrystalline are minimum. The values estimated for

https://doi.org/10.1021/acsomega.2c01136
ACS Omega 2022, 7, 15996−16012

other samples are in good agreement with the values reported in previous studies[20,49,117,118] for particles of similar sizes.

3.4. Phase Transfer to Aqueous Medium and MTT Assay. Because as-synthesized particles using the thermal decomposition method cannot be directly used in biomedical applications, they were transferred to the aqueous phase using DMSA and their biocompatibility was assessed by the MTT assay. DMSA can not only act as a stable coating molecule via chelate bonding of its carboxylate groups onto the particles' surfaces but also be further used for binding a targeting agent in biomedical applications, for example, antibodies, through its thiol group.[42] Ligand exchange was successfully performed in one sample of each group, but only the data related to sample C3, which has the highest GD of OA among all the samples is presented. After the ligand exchange, the particles in aqueous medium were highly stable, with a zeta potential of −30 mV. In addition to the calorimetric method, the concentration of the particles was also confirmed using the TGA (Figure 10). The

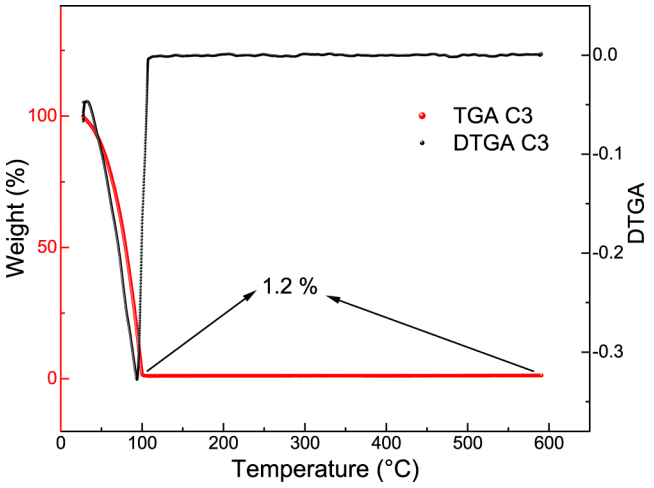

Figure 10. TGA of the sample C3 dispersed in water.

TGA result not only provides information about the dispersion concentration but also clearly demonstrates the removal of the OA from the surface of the sample. Upon the evaporation of water at around 100 °C, no change was observed in the mass of the sample, while prior to the surface modification, this sample C3 showed almost 13% weight loss.

The conversion of tetrazolium salt to formazan by a mitochondrial enzyme is referred to as the MTT assay. The outcome of this conversion can be used to verify the pharmaceutical agents' safety or toxicity on cell survival.[119] Here, the viability of two types of cell lines (NIH/3T3 and U87) was monitored at three different points (24, 48, and 72 h after their exposure to the particles). Observation (Figures S3 and S4 Supporting Information) showed that in both cell lines at low concentrations, there was no adverse effect on cell viability and negligible cell death was observed only at high concentrations. Cell death at higher concentrations (120 and 240 μM) was more pronounced for the cancerous cell line (U87) compared to NIH/3T3 cells. This different behavior can be understood based on the different metabolism and mechanism of action of the two cell lines upon nanoparticle uptake. In addition, nanoparticles' unique physicochemical properties can also show different effects on different cells. However, for an in-depth discussion on this subject, the reader is referred to refs 120−121122123124125126. Overall, we believe, based on this primary assay, these nanoparticles have great potential to be used in different biomedical applications where high saturation magnetization is a deterministic property.

4. CONCLUSIONS

In summary, for three groups of samples, we investigated the effects of solvent amount, or in other words, the concentration of reagents in the reaction (group A), the effect of the surfactant molar ratio with respect to the iron precursor (group B), and the effect of changes in the reducing agent(s) in the reaction (group C) on the structural and magnetic properties of the resulting iron oxide nanoparticles. All the other parameters such as the heating profile, the reaction atmosphere, and the stirring condition were kept constant for all the samples. A simple one-pot synthesis procedure using $Fe(acac)_3$ as the iron precursor was followed, and no vacuum condition was used during the syntheses. Two out of nine conditions studied in this work resulted in monodisperse iron oxide nanoparticles with high crystalline quality and saturation magnetization, close to bulk magnetite but having different sizes. Based on several characterization methods conducted on all the samples and comparing the results with previous reports on the thermal decomposition pathway for iron oxide nanoparticles formation, we could draw the following conclusions to understand the diverse intrinsic properties of our samples and also some controversial results on the effect of experimental conditions on the resultant particles in other studies.

Changes in the surfactant amount/type can dramatically alert the decomposition temperature of the iron precursor, which means changing the burst nucleation stage and/or nucleation and growth rates. In addition, variation in the strength of the reducing agent(s) can also have a similar effect (samples C2 and C3 in the present study, where Ol may have acted as both a surfactant and a reducing agent). Because in this study the heating profiles of all the reactions were the same, the precise separation of nucleation and growth, as the critical parameters for obtaining high-quality particles, was not probably achieved in most of the reactions. This, in turn, resulted in particles with diverse morphological and magnetic properties. If high-quality nanoparticles are considered as not only monodisperse ones but also ones that are highly crystalline and show saturation magnetization nearly equal to their bulk counterpart. Then, it may be concluded that for obtaining high-quality particles, it is hard to specify any heating rate (profile) or molar ratios between the starting materials as standard values independently. It means, for any specific heating profile, there may exist specific molar ratio(s) or vice versa that can result in high-quality iron oxide nanoparticles. This could be one of the main reasons that high-quality iron oxide nanoparticles have been reported using very different reaction parameters, particularly the heating profiles and surfactant amount. Although in the beginning some widely used parameters in the literature were chosen for this study, at the end, after a comprehensive characterization, we reached the conclusion that these parameters should not be chosen independently of each other.

■ ASSOCIATED CONTENT

Supporting Information

The Supporting Information is available free of charge at https://pubs.acs.org/doi/10.1021/acsomega.2c01136.

https://doi.org/10.1021/acsomega.2c01136
ACS Omega 2022, 7, 15996−16012

More details regarding structural characterization and the MMT assay (PDF)

AUTHOR INFORMATION

Corresponding Authors

Jae Young Lee − *School of Materials Science and Engineering, Gwangju Institute of Science and Technology, Gwangju 61005, Republic of Korea;* orcid.org/0000-0003-4493-2494; Email: jaeyounglee@gist.ac.kr

Jungwon Yoon − *Research Center for Nanorobotics in Brain, Gwangju Institute of Science and Technology, Gwangju 61005, Republic of Korea*; Email: jyoon@gist.ac.kr

Authors

Yaser Hadadian − *Research Center for Nanorobotics in Brain, Gwangju Institute of Science and Technology, Gwangju 61005, Republic of Korea; School of Integrated Technology, Gwangju Institute of Science and Technology, Gwangju 61005, Republic of Korea;* orcid.org/0000-0003-2176-2891

Hajar Masoomi − *Research Center for Nanorobotics in Brain, Gwangju Institute of Science and Technology, Gwangju 61005, Republic of Korea; School of Integrated Technology, Gwangju Institute of Science and Technology, Gwangju 61005, Republic of Korea;* orcid.org/0000-0002-5776-6141

Ali Dinari − *Research Center for Nanorobotics in Brain, Gwangju Institute of Science and Technology, Gwangju 61005, Republic of Korea; School of Integrated Technology, Gwangju Institute of Science and Technology, Gwangju 61005, Republic of Korea*

Chiseon Ryu − *School of Materials Science and Engineering, Gwangju Institute of Science and Technology, Gwangju 61005, Republic of Korea*

Seong Hwang − *School of Materials Science and Engineering, Gwangju Institute of Science and Technology, Gwangju 61005, Republic of Korea*

Seokjae Kim − *Korea Institute of Medical Microrobotics (KIMIRo), Gwangju 61011, Republic of Korea*

Beong ki Cho − *School of Materials Science and Engineering, Gwangju Institute of Science and Technology, Gwangju 61005, Republic of Korea*

Complete contact information is available at: https://pubs.acs.org/10.1021/acsomega.2c01136

Notes

The authors declare no competing financial interest.

ACKNOWLEDGMENTS

This work was supported in part by the National Research Foundation of Korea under Grant 2019M3C1B8090798, in part by the Korea Evaluation Institute of Industrial Technology under Grant 20003822, and in part by the Korea Health Industry Development Institute under Grant HI19C0642.

REFERENCES

(1) Cullity, B. D.; Graham, C. D. *Introduction to Magnetic Materials*, 2nd ed.; John Wiley & Sons, Inc.: New Jersey, 2009.

(2) Asgarian, S. M.; Shatooti, S.; Mozaffari, M. Investigation of Cation and Cation Vacancy Distributions in the Zinc Substituted Maghemite, Prepared by One Pot Room Temperature Co-precipitation Method. *J. Supercond. Nov. Magnetism* **2021**, *34*, 2933−2944.

(3) Mozaffari, M.; Shatooti, S.; Jafarzadeh, M.; Niyaifar, M.; Aftabi, A.; Mohammadpour, H.; Amiri, S. Synthesis of Zn2+ substituted maghemite nanoparticles and investigation of their structural and magnetic properties. *J. Magn. Magn. Mater.* **2015**, *382*, 366−375.

(4) Roca, A. G.; Marco, J. F.; Morales, M. d. P.; Serna, C. J. Effect of Nature and Particle Size on Properties of Uniform Magnetite and Maghemite Nanoparticles. *J. Phys. Chem. C* **2007**, *111*, 18577−18584.

(5) Santoyo Salazar, J.; Perez, L.; de Abril, O.; Truong Phuoc, L.; Ihiawakrim, D.; Vazquez, M.; Greneche, J.-M.; Begin-Colin, S.; Pourroy, G. Magnetic Iron Oxide Nanoparticles in 10−40 nm Range: Composition in Terms of Magnetite/Maghemite Ratio and Effect on the Magnetic Properties. *Chem. Mater.* **2011**, *23*, 1379−1386.

(6) Hadadian, Y.; Sampaio, D. R. T.; Ramos, A. P.; Carneiro, A. A. O.; Mozaffari, M.; Cabrelli, L. C.; Pavan, T. Z. Synthesis and characterization of zinc substituted magnetite nanoparticles and their application to magneto-motive ultrasound imaging. *J. Magn. Magn. Mater.* **2018**, *465*, 33−43.

(7) Mozaffari, M.; Hadadian, Y.; Aftabi, A.; Oveisy Moakhar, M. The effect of cobalt substitution on magnetic hardening of magnetite. *J. Magn. Magn. Mater.* **2014**, *354*, 119−124.

(8) Jang, J.-t.; Nah, H.; Lee, J.-H.; Moon, S. H.; Kim, M. G.; Cheon, J. Critical Enhancements of MRI Contrast and Hyperthermic Effects by Dopant-Controlled Magnetic Nanoparticles. *Angew. Chem.* **2009**, *121*, 1260−1264.

(9) He, S.; Zhang, H.; Liu, Y.; Sun, F.; Yu, X.; Li, X.; Zhang, L.; Wang, L.; Mao, K.; Wang, G.; Lin, Y.; Han, Z.; Sabirianov, R.; Zeng, H. Maximizing Specific Loss Power for Magnetic Hyperthermia by Hard−Soft Mixed Ferrites. *Small* **2018**, *14*, 1800135.

(10) Lee, J.-H.; Jang, J.-t.; Choi, J.-s.; Moon, S. H.; Noh, S.-h.; Kim, J.-w.; Kim, J.-G.; Kim, I.-S.; Park, K. I.; Cheon, J. Exchange-coupled magnetic nanoparticles for efficient heat induction. *Nat. Nanotechnol.* **2011**, *6*, 418−422.

(11) Wu, W.; Wu, Z.; Yu, T.; Jiang, C.; Kim, W.-S. Recent progress on magnetic iron oxide nanoparticles: synthesis, surface functional strategies and biomedical applications. *Sci. Technol. Adv. Mater.* **2015**, *16*, 023501.

(12) Park, J.; Lee, E.; Hwang, N.-M.; Kang, M.; Kim, S. C.; Hwang, Y.; Park, J.-G.; Noh, H.-J.; Kim, J.-Y.; Park, J.-H.; Hyeon, T. One-Nanometer-Scale Size-Controlled Synthesis of Monodisperse Magnetic Iron Oxide Nanoparticles. *Angew. Chem., Int. Ed.* **2005**, *44*, 2872−2877.

(13) Balakrishnan, T.; Lee, M.-J.; Dey, J.; Choi, S.-M. Sub-nanometer scale size-control of iron oxide nanoparticles with drying time of iron oleate. *CrystEngComm* **2019**, *21*, 4063−4071.

(14) Abou El-Nour, K. M. M.; Eftaiha, A. a.; Al-Warthan, A.; Ammar, R. A. A. Synthesis and applications of silver nanoparticles. *Arab. J. Chem.* **2010**, *3*, 135−140.

(15) Yeh, Y.-C.; Creran, B.; Rotello, V. M. Gold nanoparticles: preparation, properties, and applications in bionanotechnology. *Nanoscale* **2012**, *4*, 1871−1880.

(16) Wu, L.; Jubert, P.-O.; Berman, D.; Imaino, W.; Nelson, A.; Zhu, H.; Zhang, S.; Sun, S. Monolayer Assembly of Ferrimagnetic CoxFe3−xO4 Nanocubes for Magnetic Recording. *Nano Lett.* **2014**, *14*, 3395−3399.

(17) Knopp, T.; Gdaniec, N.; Möddel, M. Magnetic particle imaging: from proof of principle to preclinical applications. *Phys. Med. Biol.* **2017**, *62*, R124.

(18) Sun, S.; Zeng, H.; Robinson, D. B.; Raoux, S.; Rice, P. M.; Wang, S. X.; Li, G. Monodisperse MFe2O4 (M = Fe, Co, Mn) Nanoparticles. *J. Am. Chem. Soc.* **2004**, *126*, 273−279.

(19) Yu, W. W.; Falkner, J. C.; Yavuz, C. T.; Colvin, V. L. Synthesis of monodisperse iron oxide nanocrystals by thermal decomposition of iron carboxylate salts. *Chem. Commun.* **2004**, *20*, 2306−2307.

(20) Park, J.; An, K.; Hwang, Y.; Park, J.-G.; Noh, H.-J.; Kim, J.-Y.; Park, J.-H.; Hwang, N.-M.; Hyeon, T. Ultra-large-scale syntheses of monodisperse nanocrystals. *Nat. Mater.* **2004**, *3*, 891−895.

(21) Qiao, L.; Fu, Z.; Li, J.; Ghosen, J.; Zeng, M.; Stebbins, J.; Prasad, P. N.; Swihart, M. T. Standardizing Size- and Shape-Controlled Synthesis of Monodisperse Magnetite (Fe3O4) Nano-

https://doi.org/10.1021/acsomega.2c01136
ACS Omega 2022, 7, 15996−16012

crystals by Identifying and Exploiting Effects of Organic Impurities. *ACS Nano* **2017**, *11*, 6370−6381.
(22) Bronstein, L. M.; Huang, X.; Retrum, J.; Schmucker, A.; Pink, M.; Stein, B. D.; Dragnea, B. Influence of Iron Oleate Complex Structure on Iron Oxide Nanoparticle Formation. *Chem. Mater.* **2007**, *19*, 3624−3632.
(23) Feld, A.; Weimer, A.; Kornowski, A.; Winckelmans, N.; Merkl, J.-P.; Kloust, H.; Zierold, R.; Schmidtke, C.; Schotten, T.; Riedner, M.; Bals, S.; Weller, H. Chemistry of Shape-Controlled Iron Oxide Nanocrystal Formation. *ACS Nano* **2019**, *13*, 152−162.
(24) Qi, B.; Ye, L.; Stone, R.; Dennis, C.; Crawford, T. M.; Mefford, O. T. Influence of Ligand−Precursor Molar Ratio on the Size Evolution of Modifiable Iron Oxide Nanoparticles. *J. Phys. Chem. C* **2013**, *117*, 5429−5435.
(25) Guardia, P.; Di Corato, R.; Lartigue, L.; Wilhelm, C.; Espinosa, A.; Garcia-Hernandez, M.; Gazeau, F.; Manna, L.; Pellegrino, T. Water-Soluble Iron Oxide Nanocubes with High Values of Specific Absorption Rate for Cancer Cell Hyperthermia Treatment. *ACS Nano* **2012**, *6*, 3080−3091.
(26) Sharifi Dehsari, H.; Heidari, M.; Halda Ribeiro, A.; Tremel, W.; Jakob, G.; Donadio, D.; Potestio, R.; Asadi, K. Combined Experimental and Theoretical Investigation of Heating Rate on Growth of Iron Oxide Nanoparticles. *Chem. Mater.* **2017**, *29*, 9648−9656.
(27) Xu, Z.; Shen, C.; Hou, Y.; Gao, H.; Sun, S. Oleylamine as Both Reducing Agent and Stabilizer in a Facile Synthesis of Magnetite Nanoparticles. *Chem. Mater.* **2009**, *21*, 1778−1780.
(28) Sun, S.; Zeng, H. Size-Controlled Synthesis of Magnetite Nanoparticles. *J. Am. Chem. Soc.* **2002**, *124*, 8204−8205.
(29) Hyeon, T.; Lee, S. S.; Park, J.; Chung, Y.; Na, H. B. Synthesis of Highly Crystalline and Monodisperse Maghemite Nanocrystallites without a Size-Selection Process. *J. Am. Chem. Soc.* **2001**, *123*, 12798−12801.
(30) Sharifi Dehsari, H.; Halda Ribeiro, A.; Ersöz, B.; Tremel, W.; Jakob, G.; Asadi, K. Effect of precursor concentration on size evolution of iron oxide nanoparticles. *CrystEngComm* **2017**, *19*, 6694−6702.
(31) Moya, C.; Batlle, X.; Labarta, A. The effect of oleic acid on the synthesis of Fe3−xO4 nanoparticles over a wide size range. *Phys. Chem. Chem. Phys.* **2015**, *17*, 27373−27379.
(32) Bigioni, T. P.; Lin, X.-M.; Nguyen, T. T.; Corwin, E. I.; Witten, T. A.; Jaeger, H. M. Kinetically driven self assembly of highly ordered nanoparticle monolayers. *Nat. Mater.* **2006**, *5*, 265−270.
(33) Ariga, K.; Yamauchi, Y.; Mori, T.; Hill, J. P. 25th Anniversary Article: What Can Be Done with the Langmuir-Blodgett Method? Recent Developments and its Critical Role in Materials Science. *Adv. Mater.* **2013**, *25*, 6477−6512.
(34) Lee, D. K.; Kim, Y. H.; Kim, C. W.; Cha, H. G.; Kang, Y. S. Vast Magnetic Monolayer Film with Surfactant-Stabilized Fe3O4 Nanoparticles Using Langmuir−Blodgett Technique. *J. Phys. Chem. B* **2007**, *111*, 9288−9293.
(35) Scherrer, P. Bestimmung der inneren Struktur und der Größe von Kolloidteilchen mittels Röntgenstrahlen. In *Kolloidchemie Ein Lehrbuch*; Zsigmondy, R., Ed.; Springer Berlin Heidelberg: Berlin, Heidelberg, 1912; pp 387−409.
(36) Cullity, B. D.; Stock, S. R. *Elements of X-ray Diffraction*; Pearson New International Edition, Pearson Education Limited, 2013.
(37) Williamson, G. K.; Hall, W. H. X-ray line broadening from filed aluminium and wolfram. *Acta Metall.* **1953**, *1*, 22−31.
(38) Köhler, T.; Feoktystov, A.; Petracic, O.; Kentzinger, E.; Bhatnagar-Schöffmann, T.; Feygenson, M.; Nandakumaran, N.; Landers, J.; Wende, H.; Cervellino, A.; Rücker, U.; Kovács, A.; Dunin-Borkowski, R. E.; Brückel, T. Mechanism of magnetization reduction in iron oxide nanoparticles. *Nanoscale* **2021**, *13*, 6965−6976.
(39) Cohen, M. U. Precision Lattice Constants from X-Ray Powder Photographs. *Rev. Sci. Instrum.* **1935**, *6*, 68−74.
(40) Nekvapil, F.; Bunge, A.; Radu, T.; Cinta Pinzaru, S.; Turcu, R. Raman spectra tell us so much more: Raman features and saturation magnetization for efficient analysis of manganese zinc ferrite nanoparticles. *J. Raman Spectrosc.* **2020**, *51*, 959−968.
(41) Herbst, J. F.; Pinkerton, F. E. Law of approach to saturation for polycrystalline ferromagnets: Remanent initial state. *Phys. Rev. B: Condens. Matter Mater. Phys.* **1998**, *57*, 10733−10739.
(42) Jun, Y.-w.; Huh, Y.-M.; Choi, J.-s.; Lee, J.-H.; Song, H.-T.; Kim, S.; Yoon, S.; Kim, K.-S.; Shin, J.-S.; Suh, J.-S.; Cheon, J. Nanoscale Size Effect of Magnetic Nanocrystals and Their Utilization for Cancer Diagnosis via Magnetic Resonance Imaging. *J. Am. Chem. Soc.* **2005**, *127*, 5732−5733.
(43) LaMer, V. K.; Dinegar, R. H. Theory, Production and Mechanism of Formation of Monodispersed Hydrosols. *J. Am. Chem. Soc.* **1950**, *72*, 4847−4854.
(44) Thanh, N. T. K.; Maclean, N.; Mahiddine, S. Mechanisms of Nucleation and Growth of Nanoparticles in Solution. *Chem. Rev.* **2014**, *114*, 7610−7630.
(45) Zeng, H.; Rice, P. M.; Wang, S. X.; Sun, S. Shape-Controlled Synthesis and Shape-Induced Texture of MnFe2O4 Nanoparticles. *J. Am. Chem. Soc.* **2004**, *126*, 11458−11459.
(46) Vargas, J. M.; Zysler, R. D. Tailoring the size in colloidal iron oxide magnetic nanoparticles. *Nanotechnology* **2005**, *16*, 1474−1476.
(47) Baaziz, W.; Pichon, B. P.; Fleutot, S.; Liu, Y.; Lefevre, C.; Greneche, J.-M.; Toumi, M.; Mhiri, T.; Begin-Colin, S. Magnetic Iron Oxide Nanoparticles: Reproducible Tuning of the Size and Nanosized-Dependent Composition, Defects, and Spin Canting. *J. Phys. Chem. C* **2014**, *118*, 3795−3810.
(48) Guardia, P.; Pérez, N.; Labarta, A.; Batlle, X. Controlled Synthesis of Iron Oxide Nanoparticles over a Wide Size Range. *Langmuir* **2010**, *26*, 5843−5847.
(49) Demortière, A.; Panissod, P.; Pichon, B. P.; Pourroy, G.; Guillon, D.; Donnio, B.; Bégin-Colin, S. Size-dependent properties of magnetic iron oxide nanocrystals. *Nanoscale* **2011**, *3*, 225−232.
(50) Meledandri, C. J.; Stolarczyk, J. K.; Ghosh, S.; Brougham, D. F. Nonaqueous Magnetic Nanoparticle Suspensions with Controlled Particle Size and Nuclear Magnetic Resonance Properties. *Langmuir* **2008**, *24*, 14159−14165.
(51) Zhu, Y.; Jiang, F. Y.; Chen, K.; Kang, F.; Tang, Z. K. Size-controlled synthesis of monodisperse superparamagnetic iron oxide nanoparticles. *J. Alloys Compd.* **2011**, *509*, 8549−8553.
(52) Hufschmid, R.; Arami, H.; Ferguson, R. M.; Gonzales, M.; Teeman, E.; Brush, L. N.; Browning, N. D.; Krishnan, K. M. Synthesis of phase-pure and monodisperse iron oxide nanoparticles by thermal decomposition. *Nanoscale* **2015**, *7*, 11142−11154.
(53) Yin, M.; Willis, A.; Redl, F.; Turro, N. J.; O'Brien, S. P. Influence of Capping Groups on the Synthesis of γ-Fe2O3 Nanocrystals. *J. Mater. Res.* **2004**, *19*, 1208−1215.
(54) Hyeon, T. Chemical synthesis of magnetic nanoparticles. *Chem. Commun.* **2003**, *8*, 927−934.
(55) Park, J.; Joo, J.; Kwon, S. G.; Jang, Y.; Hyeon, T. Synthesis of Monodisperse Spherical Nanocrystals. *Angew. Chem., Int. Ed.* **2007**, *46*, 4630−4660.
(56) Salas, G.; Casado, C.; Teran, F. J.; Miranda, R.; Serna, C. J.; Morales, M. P. Controlled synthesis of uniform magnetite nanocrystals with high-quality properties for biomedical applications. *J. Mater. Chem.* **2012**, *22*, 21065−21075.
(57) Guardia, P.; Labarta, A.; Batlle, X. Tuning the Size, the Shape, and the Magnetic Properties of Iron Oxide Nanoparticles. *J. Phys. Chem. C* **2011**, *115*, 390−396.
(58) da Silva, S. W.; Melo, T. F. O.; Soler, M. A. G.; Lima, E. C. D.; da Silva, M. F.; Morais, P. C. Stability of citrate-coated magnetite and cobalt-ferrite nanoparticles under laser irradiation: a Raman spectroscopy investigation. *IEEE Trans. Magn.* **2003**, *39*, 2645−2647.
(59) de Faria, D. L. A.; Venâncio Silva, S.; de Oliveira, M. T. Raman microspectroscopy of some iron oxides and oxyhydroxides. *J. Raman Spectrosc.* **1997**, *28*, 873−878.
(60) Li, Y.-S.; Church, J. S.; Woodhead, A. L. Infrared and Raman spectroscopic studies on iron oxide magnetic nano-particles and their surface modifications. *J. Magn. Magn. Mater.* **2012**, *324*, 1543−1550.

https://doi.org/10.1021/acsomega.2c01136
ACS Omega 2022, 7, 15996−16012

(61) Hanesch, M. Raman spectroscopy of iron oxides and (oxy)hydroxides at low laser power and possible applications in environmental magnetic studies. *Geophys. J. Int.* **2009**, *177*, 941−948.
(62) Testa-Anta, M.; Ramos-Docampo, M. A.; Comesaña-Hermo, M.; Rivas-Murias, B.; Salgueiriño, V. Raman spectroscopy to unravel the magnetic properties of iron oxide nanocrystals for bio-related applications. *Nanoscale Adv.* **2019**, *1*, 2086−2103.
(63) Kertmen, A.; Torruella, P.; Coy, E.; Yate, L.; Nowaczyk, G.; Gapiński, J.; Vogt, C.; Toprak, M.; Estradé, S.; Peiró, F.; Milewski, S.; Jurga, S.; Andruszkiewicz, R. Acetate-Induced Disassembly of Spherical Iron Oxide Nanoparticle Clusters into Monodispersed Core−Shell Structures upon Nanoemulsion Fusion. *Langmuir* **2017**, *33*, 10351−10365.
(64) Chamritski, I.; Burns, G. Infrared- and Raman-Active Phonons of Magnetite, Maghemite, and Hematite: A Computer Simulation and Spectroscopic Study. *J. Phys. Chem. B* **2005**, *109*, 4965−4968.
(65) Waldron, R. D. Infrared Spectra of Ferrites. *Phys. Rev.* **1955**, *99*, 1727−1735.
(66) Zhang, J. L.; Srivastava, R. S.; Misra, R. D. K. Core−Shell Magnetite Nanoparticles Surface Encapsulated with Smart Stimuli-Responsive Polymer: Synthesis, Characterization, and LCST of Viable Drug-Targeting Delivery System. *Langmuir* **2007**, *23*, 6342−6351.
(67) Yamaura, M.; Camilo, R. L.; Sampaio, L. C.; Macêdo, M. A.; Nakamura, M.; Toma, H. E. Preparation and characterization of (3-aminopropyl)triethoxysilane-coated magnetite nanoparticles. *J. Magn. Magn. Mater.* **2004**, *279*, 210−217.
(68) Patil, R. M.; Shete, P. B.; Thorat, N. D.; Otari, S. V.; Barick, K. C.; Prasad, A.; Ningthoujam, R. S.; Tiwale, B. M.; Pawar, S. H. Non-aqueous to aqueous phase transfer of oleic acid coated iron oxide nanoparticles for hyperthermia application. *RSC Adv.* **2014**, *4*, 4515−4522.
(69) Zhang, L.; He, R.; Gu, H.-C. Oleic acid coating on the monodisperse magnetite nanoparticles. *Appl. Surf. Sci.* **2006**, *253*, 2611−2617.
(70) Can, M. M.; Ozcan, S.; Ceylan, A.; Firat, T. Effect of milling time on the synthesis of magnetite nanoparticles by wet milling. *Mater. Sci. Eng., B* **2010**, *172*, 72−75.
(71) Ma, M.; Zhang, Y.; Yu, W.; Shen, H.-y.; Zhang, H.-q.; Gu, N. Preparation and characterization of magnetite nanoparticles coated by amino silane. *Colloids Surf., A* **2003**, *212*, 219−226.
(72) Sundar, S.; Mariappan, R.; Piraman, S. Synthesis and characterization of amine modified magnetite nanoparticles as carriers of curcumin-anticancer drug. *Powder Technol.* **2014**, *266*, 321−328.
(73) Zheng, L.; Su, W.; Qi, Z.; Xu, Y.; Zhou, M.; Xie, Y. First-order metal−insulator transition and infrared identification of shape-controlled magnetite nanocrystals. *Nanotechnology* **2011**, *22*, 485706.
(74) Nasrazadani, S.; Raman, A. The application of infrared spectroscopy to the study of rust systems—II. Study of cation deficiency in magnetite (Fe3O4) produced during its transformation to maghemite (γ-Fe2O3) and hematite (α-Fe2O3). *Corros. Sci.* **1993**, *34*, 1355−1365.
(75) Sharifi Dehsari, H.; Ksenofontov, V.; Möller, A.; Jakob, G.; Asadi, K. Determining Magnetite/Maghemite Composition and Core−Shell Nanostructure from Magnetization Curve for Iron Oxide Nanoparticles. *J. Phys. Chem. C* **2018**, *122*, 28292−28301.
(76) Frison, R.; Cernuto, G.; Cervellino, A.; Zaharko, O.; Colonna, G. M.; Guagliardi, A.; Masciocchi, N. Magnetite−Maghemite Nanoparticles in the 5−15 nm Range: Correlating the Core−Shell Composition and the Surface Structure to the Magnetic Properties. A Total Scattering Study. *Chem. Mater.* **2013**, *25*, 4820−4827.
(77) Klotz, M.; Ayral, A.; Guizard, C.; Ménager, C.; Cabuil, V. Silica Coating on Colloidal Maghemite Particles. *J. Colloid Interface Sci.* **1999**, *220*, 357−361.
(78) Daou, T. J.; Grenèche, J. M.; Pourroy, G.; Buathong, S.; Derory, A.; Ulhaq-Bouillet, C.; Donnio, B.; Guillon, D.; Begin-Colin, S. Coupling Agent Effect on Magnetic Properties of Functionalized Magnetite-Based Nanoparticles. *Chem. Mater.* **2008**, *20*, 5869−5875.
(79) Bu, W.; Chen, Z.; Chen, F.; Shi, J. Oleic Acid/Oleylamine Cooperative-Controlled Crystallization Mechanism for Monodisperse Tetragonal Bipyramid NaLa(MoO4)2 Nanocrystals. *J. Phys. Chem. C* **2009**, *113*, 12176−12185.
(80) Harris, R. A.; Shumbula, P. M.; van der Walt, H. Analysis of the Interaction of Surfactants Oleic Acid and Oleylamine with Iron Oxide Nanoparticles through Molecular Mechanics Modeling. *Langmuir* **2015**, *31*, 3934−3943.
(81) El Mendili, Y.; Grasset, F.; Randrianantoandro, N.; Nerambourg, N.; Greneche, J.-M.; Bardeau, J.-F. Improvement of Thermal Stability of Maghemite Nanoparticles Coated with Oleic Acid and Oleylamine Molecules: Investigations under Laser Irradiation. *J. Phys. Chem. C* **2015**, *119*, 10662−10668.
(82) Treadwell, L. J.; Boyle, T. J.; Bell, N. S.; Rodriguez, M. A.; Muntifering, B. R.; Hattar, K. Impact of oleylamine: oleic acid ratio on the morphology of yttria nanomaterials. *J. Mater. Sci.* **2017**, *52*, 8268−8279.
(83) Nakamoto, K. *Infrared and Raman Spectra of Inorganic and Coordination Compounds Part B: Applications in Coordination, Organometallic, and Bioinorganic Chemistry*; John Wiley & Sons, 2009.
(84) Deacon, G.; Phillips, R. J. Relationships between the carbon-oxygen stretching frequencies of carboxylato complexes and the type of carboxylate coordination. *Coord. Chem. Rev.* **1980**, *33*, 227−250.
(85) Lu, Y.; Miller, J. D. Carboxyl Stretching Vibrations of Spontaneously Adsorbed and LB-Transferred Calcium Carboxylates as Determined by FTIR Internal Reflection Spectroscopy. *J. Colloid Interface Sci.* **2002**, *256*, 41−52.
(86) Bixner, O.; Lassenberger, A.; Baurecht, D.; Reimhult, E. Complete Exchange of the Hydrophobic Dispersant Shell on Monodisperse Superparamagnetic Iron Oxide Nanoparticles. *Langmuir* **2015**, *31*, 9198−9204.
(87) Bronstein, L. M.; Atkinson, J. E.; Malyutin, A. G.; Kidwai, F.; Stein, B. D.; Morgan, D. G.; Perry, J. M.; Karty, J. A. Nanoparticles by Decomposition of Long Chain Iron Carboxylates: From Spheres to Stars and Cubes. *Langmuir* **2011**, *27*, 3044−3050.
(88) Wang, Y.; Du, X.; Guo, L.; Liu, H. Chain orientation and headgroup structure in Langmuir monolayers of stearic acid and metal stearate (Ag, Co, Zn, and Pb) studied by infrared reflection-absorption spectroscopy. *J. Chem. Phys.* **2006**, *124*, 134706.
(89) Edwards, D. A.; Hayward, R. N. Transition metal acetates. *Can. J. Chem.* **1968**, *46*, 3443−3446.
(90) Simon-Kutscher, J.; Gericke, A.; Hühnerfuss, H. Effect of Bivalent Ba, Cu, Ni, and Zn Cations on the Structure of Octadecanoic Acid Monolayers at the Air−Water Interface As Determined by External Infrared Reflection−Absorption Spectroscopy. *Langmuir* **1996**, *12*, 1027−1034.
(91) Hadjiivanov, K. I.; Panayotov, D. A.; Mihaylov, M. Y.; Ivanova, E. Z.; Chakarova, K. K.; Andonova, S. M.; Drenchev, N. L. Power of Infrared and Raman Spectroscopies to Characterize Metal-Organic Frameworks and Investigate Their Interaction with Guest Molecules. *Chem. Rev.* **2021**, *121*, 1286−1424.
(92) Ralandinliu Kahmei, R. D.; Borah, J. P. Clustering of MnFe 2 O 4 nanoparticles and the effect of field intensity in the generation of heat for hyperthermia application. *Nanotechnology* **2019**, *30*, 035706.
(93) Roca, A. G.; Morales, M. P.; Serna, C. J. Synthesis of Monodispersed Magnetite Particles From Different Organometallic Precursors. *IEEE Trans. Magn.* **2006**, *42*, 3025−3029.
(94) Patil, R. M.; Shete, P. B.; Thorat, N. D.; Otari, S. V.; Barick, K. C.; Prasad, A.; Ningthoujam, R. S.; Tiwale, B. M.; Pawar, S. H. Superparamagnetic iron oxide/chitosan core/shells for hyperthermia application: Improved colloidal stability and biocompatibility. *J. Magn. Magn. Mater.* **2014**, *355*, 22−30.
(95) Dallas, P.; Bourlinos, A. B.; Niarchos, D.; Petridis, D. Synthesis of tunable sized capped magnetic iron oxide nanoparticles highly soluble in organic solvents. *J. Mater. Sci.* **2007**, *42*, 4996−5002.
(96) Wang, S.; Niu, R.; Yang, Y.; Zhou, X.; Luo, S.; Zhang, C.; Wang, Y. Aptamer-functionalized chitosan magnetic nanoparticles as a novel adsorbent for selective extraction of ochratoxin A. *Int. J. Biol. Macromol.* **2020**, *153*, 583−590.
(97) Lu, X.; Tuan, H.-Y.; Chen, J.; Li, Z.-Y.; Korgel, B. A.; Xia, Y. Mechanistic Studies on the Galvanic Replacement Reaction between

https://doi.org/10.1021/acsomega.2c01136
ACS Omega 2022, 7, 15996−16012

Multiply Twinned Particles of Ag and HAuCl4 in an Organic Medium. *J. Am. Chem. Soc.* **2007**, *129*, 1733−1742.
(98) Seyhan, M.; Kucharczyk, W.; Yarar, U. E.; Rickard, K.; Rende, D.; Baysal, N.; Bucak, S.; Ozisik, R. Interfacial surfactant competition and its impact on poly(ethylene oxide)/Au and poly(ethylene oxide)/Ag nanocomposite properties. *Nanotechnol. Sci. Appl.* **2017**, *10*, 69−77.
(99) Baharuddin, A. A.; Ang, B. C.; Abu Hussein, N. A.; Andriyana, A.; Wong, Y. H. Mechanisms of highly stabilized ex-situ oleic acid-modified iron oxide nanoparticles functionalized with 4-pentynoic acid. *Mater. Chem. Phys.* **2018**, *203*, 212−222.
(100) Sharifi Dehsari, H.; Harris, R. A.; Ribeiro, A. H.; Tremel, W.; Asadi, K. Optimizing the Binding Energy of the Surfactant to Iron Oxide Yields Truly Monodisperse Nanoparticles. *Langmuir* **2018**, *34*, 6582−6590.
(101) Castellanos-Rubio, I.; Insausti, M.; Garaio, E.; Gil de Muro, I.; Plazaola, F.; Rojo, T.; Lezama, L. Fe3O4 nanoparticles prepared by the seeded-growth route for hyperthermia: electron magnetic resonance as a key tool to evaluate size distribution in magnetic nanoparticles. *Nanoscale* **2014**, *6*, 7542−7552.
(102) Perez De Berti, I. O.; Cagnoli, M. V.; Pecchi, G.; Alessandrini, J. L.; Stewart, S. J.; Bengoa, J. F.; Marchetti, S. G. Alternative low-cost approach to the synthesis of magnetic iron oxide nanoparticles by thermal decomposition of organic precursors. *Nanotechnology* **2013**, *24*, 175601.
(103) Petracic, O. Superparamagnetic nanoparticle ensembles. *Superlattices Microstruct.* **2010**, *47*, 569−578.
(104) Shavel, A.; Rodríguez-González, B.; Pacifico, J.; Spasova, M.; Farle, M.; Liz-Marzán, L. M. Shape Control in Iron Oxide Nanocrystal Synthesis, Induced by Trioctylammonium Ions. *Chem. Mater.* **2009**, *21*, 1326−1332.
(105) Nedelkoski, Z.; Kepaptsoglou, D.; Lari, L.; Wen, T.; Booth, R. A.; Oberdick, S. D.; Galindo, P. L.; Ramasse, Q. M.; Evans, R. F. L.; Majetich, S.; Lazarov, V. K. Origin of reduced magnetization and domain formation in small magnetite nanoparticles. *Sci. Rep.* **2017**, *7*, 45997.
(106) Kemp, S. J.; Ferguson, R. M.; Khandhar, A. P.; Krishnan, K. M. Monodisperse magnetite nanoparticles with nearly ideal saturation magnetization. *RSC Adv.* **2016**, *6*, 77452−77464.
(107) Cooper, S. R.; Plummer, L. K.; Cosby, A. G.; Lenox, P.; Jander, A.; Dhagat, P.; Hutchison, J. E. Insights into the Magnetic Properties of Sub-10 nm Iron Oxide Nanocrystals through the Use of a Continuous Growth Synthesis. *Chem. Mater.* **2018**, *30*, 6053−6062.
(108) Kandasamy, G.; Maity, D. Recent advances in superparamagnetic iron oxide nanoparticles (SPIONs) for in vitro and in vivo cancer nanotheranostics. *Int. J. Pharm.* **2015**, *496*, 191−218.
(109) Guardia, P.; Batlle-Brugal, B.; Roca, A. G.; Iglesias, O.; Morales, M. P.; Serna, C. J.; Labarta, A.; Batlle, X. Surfactant effects in magnetite nanoparticles of controlled size. *J. Magn. Magn. Mater.* **2007**, *316*, e756−e759.
(110) de Montferrand, C.; Hu, L.; Lalatonne, Y.; Lièvre, N.; Bonnin, D.; Brioude, A.; Motte, L. SiO2 versus chelating agent@ iron oxide nanoparticles: interactions effect in nanoparticles assemblies at low magnetic field. *J. Sol-Gel Sci. Technol.* **2015**, *73*, 572−579.
(111) McKenna, K. P.; Hofer, F.; Gilks, D.; Lazarov, V. K.; Chen, C.; Wang, Z.; Ikuhara, Y. Atomic-scale structure and properties of highly stable antiphase boundary defects in Fe3O4. *Nat. Commun.* **2014**, *5*, 5740.
(112) Parkinson, G. S.; Manz, T. A.; Novotný, Z.; Sprunger, P. T.; Kurtz, R. L.; Schmid, M.; Sholl, D. S.; Diebold, U. Antiphase domain boundaries at the $Fe_3O_4(001)$ surface. *Phys. Rev. B: Condens. Matter Mater. Phys.* **2012**, *85*, 195450.
(113) Fontaiña-Troitiño, N.; Ramos-Docampo, M. A.; Testa-Anta, M.; Rodríguez-González, B.; Bañobre-López, M.; Bocher, L.; McKenna, K. P.; Salgueiriño, V. Antiphase boundaries in truncated octahedron-shaped Zn-doped magnetite nanocrystals. *J. Mater. Chem. C* **2018**, *6*, 12800−12807.
(114) Kale, A.; Gubbala, S.; Misra, R. D. K. Magnetic behavior of nanocrystalline nickel ferrite synthesized by the reverse micelle technique. *J. Magn. Magn. Mater.* **2004**, *277*, 350−358.
(115) Bødker, F.; Mørup, S.; Linderoth, S. Surface effects in metallic iron nanoparticles. *Phys. Rev. Lett.* **1994**, *72*, 282−285.
(116) Liu, B. H.; Ding, J. Strain-induced high coercivity in CoFe[sub 2]O[sub 4] powders. *Appl. Phys. Lett.* **2006**, *88*, 042506.
(117) Lima, E.; Brandl, A. L.; Arelaro, A. D.; Goya, G. F. Spin disorder and magnetic anisotropy in Fe3O4 nanoparticles. *J. Appl. Phys.* **2006**, *99*, 083908.
(118) Hadadian, Y.; Ramos, A. P.; Pavan, T. Z. Role of zinc substitution in magnetic hyperthermia properties of magnetite nanoparticles: interplay between intrinsic properties and dipolar interactions. *Sci. Rep.* **2019**, *9*, 18048.
(119) Hansen, M. B.; Nielsen, S. E.; Berg, K. Re-examination and further development of a precise and rapid dye method for measuring cell growth/cell kill. *J. Immunol. Methods* **1989**, *119*, 203−210.
(120) Peng, J.; Yang, Q.; Shi, K.; Xiao, Y.; Wei, X.; Qian, Z. Intratumoral fate of functional nanoparticles in response to microenvironment factor: Implications on cancer diagnosis and therapy. *Adv. Drug Delivery Rev.* **2019**, *143*, 37−67.
(121) Webb, B. A.; Chimenti, M.; Jacobson, M. P.; Barber, D. L. Dysregulated pH: a perfect storm for cancer progression. *Nat. Rev. Cancer* **2011**, *11*, 671−677.
(122) De Wever, O.; Demetter, P.; Mareel, M.; Bracke, M. Stromal myofibroblasts are drivers of invasive cancer growth. *Int. J. Cancer* **2008**, *123*, 2229−2238.
(123) Hynes, R. O.; Naba, A. Overview of the matrisome—an inventory of extracellular matrix constituents and functions. *Cold Spring Harbor Perspect. Biol.* **2012**, *4*, a004903.
(124) Frantz, C.; Stewart, K. M.; Weaver, V. M. The extracellular matrix at a glance. *J. Cell Sci.* **2010**, *123*, 4195−4200.
(125) Bai Aswathanarayan, J.; Rai Vittal, R.; Muddegowda, U. Anticancer activity of metal nanoparticles and their peptide conjugates against human colon adenorectal carcinoma cells. *Artif. Cell Nanomed. Biotechnol.* **2018**, *46*, 1444−1451.
(126) Caputo, F.; De Nicola, M.; Ghibelli, L. Pharmacological potential of bioactive engineered nanomaterials. *Biochem. Pharmacol.* **2014**, *92*, 112−130.

https://doi.org/10.1021/acsomega.2c01136
ACS Omega 2022, 7, 15996−16012